



HAL
open science

Single Residue Variation in Skeletal Muscle Myosin Enables Direct and Selective Drug Targeting for Spasticity and Muscle Stiffness

Máté Gyimesi, Ádám Horváth, Demeter Túrós, Sharad Kumar Suthar, Máté Péntzes, Csilla Kurdi, Louise Canon, Carlos Kikuti, Kathleen Ruppel, Darshan Trivedi, et al.

► **To cite this version:**

Máté Gyimesi, Ádám Horváth, Demeter Túrós, Sharad Kumar Suthar, Máté Péntzes, et al.. Single Residue Variation in Skeletal Muscle Myosin Enables Direct and Selective Drug Targeting for Spasticity and Muscle Stiffness. *Cell*, 2020, 183 (2), pp.335-346.e13. 10.1016/j.cell.2020.08.050 . hal-03453772

HAL Id: hal-03453772

<https://hal.science/hal-03453772>

Submitted on 29 Nov 2021

HAL is a multi-disciplinary open access archive for the deposit and dissemination of scientific research documents, whether they are published or not. The documents may come from teaching and research institutions in France or abroad, or from public or private research centers.

L'archive ouverte pluridisciplinaire **HAL**, est destinée au dépôt et à la diffusion de documents scientifiques de niveau recherche, publiés ou non, émanant des établissements d'enseignement et de recherche français ou étrangers, des laboratoires publics ou privés.

Single residue variation in skeletal muscle myosin enables selective targeting: a small-molecule inhibitor ameliorates spastic gait disorder

Máté Gyimesi^{1,2}, Ádám I. Horváth¹, Demeter Túrós¹, Sharad Kumar Suthar³, Máté Péntzes¹, Csilla Kurdi¹, Louise Canon⁴, Carlos Kikutí⁴, Kathleen M. Ruppel⁵, Darshan V. Trivedi⁵, James A. Spudich⁵, István Lőrincz³, Anna Á. Rauscher^{1,2}, Mihály Kovács^{1,6}, Endre Pál⁷, Sámuel Komoly⁷, Anne Houdusse⁴, András Málnási-Csizmadia^{1,6,*}

¹MTA-ELTE Motor Pharmacology Research Group, Pázmány Péter sétány 1/c, H-1117 Budapest, Hungary

²Optopharma Ltd., Szilágyi Erzsébet fasor 27., H-1026 Budapest, Hungary

³Printnet Ltd., Kisgömb utca 25-27., H-1135 Budapest, Hungary

⁴Structural Motility, Institut Curie, Paris Université Sciences et Lettres, Sorbonne Université, CNRS UMR144, 75005 Paris

⁵Department of Biochemistry, Stanford University School of Medicine, Beckman Center B400, 279 W. Campus Drive, Stanford, CA 94305, USA

⁶Department of Biochemistry, Eötvös Loránd University, Pázmány Péter sétány 1/c, H-1117 Budapest, Hungary and Brunszvik u. 2., H-2462 Martonvásár, Hungary

⁷Department of Neurology, University of Pécs, Rét utca 2., H-7623 Pécs, Hungary

*Correspondence to: András Málnási-Csizmadia, malna@elte.hu, ELTE Eötvös Loránd University, Department of Biochemistry, Pázmány Péter sétány 1/c, 1117 Budapest, Hungary, Tel: +36-1-372-2500

Summary

Muscle spasticity after nervous system injuries and painful low back spasm affect more than 10% of global population. Current medications are of limited efficacy and cause neurological and cardiovascular side effects due to targeting upstream regulators of muscle contraction. Direct myosin inhibition could provide optimal muscle relaxation, however, targeting skeletal myosin is particularly challenging because of its high sequential and structural similarity to cardiac isoform. We identified a key residue difference between these myosin isoforms in the communication center of the functional regions, which allowed us to design a selective inhibitor, MPH-220, tested on animal and human samples. Mutagenic analysis and the atomic structure of MPH-220-bound skeletal muscle myosin confirmed the mechanism of specificity. Targeting skeletal muscle myosin by MPH-220 enabled muscle relaxation without cardiovascular side effects and improved spastic gait disorders after brain injury in disease animal model. MPH-220 provides potential nervous system-independent therapies for spasticity and muscle stiffness.

Introduction

Spasticity – characterized by involuntary increased tone of skeletal muscles – is a common sensorimotor disorder in patients with brain and spinal cord injuries after stroke, trauma, cerebral palsy, or in multiple sclerosis and several myopathies of different etiologies (Li, 2017; Trompetto et al., 2014). Spasticity-related physical and mental conditions of patients often permanently disable self-supporting life management and ability to work (Martin et al., 2014; Rychlik et al., 2016). **Economic burden** for post-stroke patients with spasticity are 4-fold higher than those for patients without spasticity (Zorowitz et al., 2013), **which includes direct costs of medications and hospitalization and indirect costs of caregiver assignments and independent daily life facilitating instruments.**

Spasticity develops as a consequence of complex rearrangements of supraspinal inputs, which transforms the synaptic regulation of motoneurons that drives muscle contraction. The resulting exaggerated stretch reflex is accompanied with disrupted balance in regulation from the premotor cortex and reticular formation of the brainstem, which finally leads to aberrantly increased potentiation of motoneurons and hypercontraction of muscles (Enslin et al., 2020; Mukherjee and Chakravarty, 2010; Trompetto et al., 2014).

Current muscle relaxants in medical practice target the central nervous system (e.g. baclofen (GABA_B agonist) and tizanidine (α 2 agonist)), the neuromuscular junction (botulinum toxins) or the sarcoplasmic reticulum in muscle cells (dantrolene) (**Fig. 1A**). Due to their aspecific mechanism of action centrally acting muscle relaxants have a wide range of neurological and cardiovascular side effects (drowsiness, dizziness, depression, low blood pressure) (Meleger, 2006; Smit and Slim, 2008), and low levels of efficacy (Orsnes et al., 2000), which often necessitates the application of an intrathecal pump surgically implanted inside the body (Medical Advisory, 2005). Systemic treatment with botulinum toxins is impossible due to their lethal effect on respiratory and cardiac functions, and local treatments are painful, costly and often ineffective (Careta et al., 2015; Pavone et al., 2016). Dantrolene has been associated with severe hepatotoxicity and genotoxicity (NIH, 2012), therefore its clinical use is now restricted to life-threatening malignant hyperthermia. Surgical treatment of severe spasticity is limited to selective dorsal rhizotomy, when the sensory roots that transfer abnormal information from the muscles to the spinal cord are transected. However, the advantage of dorsal rhizotomy over oral medications is only marginal, because the treatment often leads to paralysis, chronic back pain, sensory dysfunction, inflammation, constipation and cyst formation in the spinal column (cf. NICE interventional guidance 373).

Besides nervous system injury related spasticity, permanent muscle spasms emerge as the leading source of prolonged pain in non-specific low back pain and chronic musculoskeletal pain disorder, fibromyalgia, altogether affecting more than 10% of global population (Marques et al., 2017; Vos et al., 2012). Although treatments of muscle spasm in these syndromes with systemic muscle relaxants are statistically effective, recommendations for their use in clinics underline

precautions due to the reported adverse side effects resulting from non-specific targeting of the nervous system (Tofferi et al., 2004; van Tulder et al., 2003).

These considerations emphasize the unmet medical need for the development of a new-generation anti-spastic drug, which directly targets the effector protein of muscle contraction while avoiding neurological and cardiovascular side effects. Nervous system independent inhibition of muscle contraction in spastic patients could also overcome the need for targeting the otherwise disrupted synaptic balance of neuronal regulation.

Selective inhibition of skeletal muscles, however, raises the challenge of developing a small molecule that distinguishes between the structurally and sequentially highly similar myosin-2 isoforms. The ideal candidate inhibits only fast skeletal muscle fast isoforms (MyHC IIA,b,x/d), because the slow isoform in skeletal muscles (myosin heavy chain, MyHC I) expressed from the *MYH7* gene is identical to β -cardiac myosin, the most abundant motor in the ventricles of the heart (Coluccio, 2020) (Fig. 1B, Fig S1).

Results

In order to relax muscle fibers, we aimed to arrest the actomyosin force generation cycle in the actin-detached weak actin-binding state (Takacs et al., 2010), when myosin heads are decoupled from actin filaments (Malnasi-Csizmadia and Kovacs, 2010; Sweeney and Hammers, 2018) (Fig. 1C). Using rational pharmacological design in a model MyHC IIA myosin structure we developed and optimized a small-molecule inhibitor (MPH-220) into the myosin-2 class specific blebbistatin-binding pocket (Allingham et al., 2005; Kovacs et al., 2004; Limouze et al., 2004; Straight et al., 2003) (Fig. 1D, Fig. S2). MPH-220 enabled selective inhibition of fast skeletal myosin-2 isoforms (further referred to as skeletal myosins, Fig. S1) isolated from rabbit psoas muscle, while – even at extremely high concentrations – it did not inhibit the ATPase activity of slow skeletal/ β -cardiac myosin (further referred to as cardiac myosin) isolated from left ventricle of porcine heart nor smooth muscle myosin-2 (Fig. 1E, Table S1), nor any non-muscle myosin-2 (NM2) isoforms (Fig. 1F, Table S1). Sequence analysis of the inhibitor binding site revealed an important difference between the cardiac and skeletal myosins near the morpholine ring of MPH-220 at a location playing a key role in the myosin force generation pathway (Malnasi-Csizmadia and Kovacs, 2010). The drug-interacting amino acid is uniquely and invariably leucine in **fast skeletal myosin heavy chains** (Leu⁴⁷⁶ in human MyHC IIA), while this position is occupied by phenylalanine in all other myosin-2 isoforms (Fig. 1B, Fig. S1). We hypothesized that this structural difference can be the basis for the extreme selectivity of MPH-220 toward skeletal myosins. Therefore we assessed the role of a Phe/Leu exchange through mutational analysis of human non-muscle myosin-2C (NM2C), which is not inhibited by MPH-220 in the wild-type form possibly due to the presence of Phe⁴⁹⁰ in the corresponding position. According to our hypothesis the expressed NM2C^{F490L} variant became sensitive to MPH-220 (Fig. 1F, Fig. S3), corroborating that the single amino acid change determines the observed selectivity.

Considering the selective inhibitory nature of MPH-220 on myosin samples (Fig. 1E-F), and its potential to become a new-generation anti-spastic drug candidate we performed ATPase

inhibition assays on human myosin samples. Expressed human β -cardiac myosin was essentially unaffected by MPH-220, while the non-selective myosin-2 inhibitor, blebbistatin, completely blocked its ATPase activity (**Fig. 1G**, **Table S1**). We further tested MPH-220 on skeletal and cardiac myosin samples isolated from patient-derived biopsies (**Fig. 1H**, **Table S1**). In line with their myosin-2 isoform composition, skeletal myosin samples from *m.vastus lateralis* and *m.soleus* – containing 56% and 28% fast isoforms in human muscles (**Fig. S4**) – were inhibited by 70% and 29%, respectively, confirming the hypothesis that only the fast isoform fraction is targeted by MPH-220. More importantly, β -cardiac myosin isolated from human heart left ventricle was unaffected by MPH-220 (**Fig. 1H**, **Table S1**). By contrast, blebbistatin reduced the activity of *m.vastus lateralis* and cardiac myosin samples by more than 90%, confirming that MPH-220 inhibition is proportional to the ratio of fast myosin isoform in different tissues (**Fig. 1H**, **Table S1**). These results provide the basis for future safe systemic administration of MPH-220 to human patients. **Left ventricle human biopsy contains cca. 10% α -cardiac myosin isoform (expressed from the *MYH6* gene (**Fig. S1**)) (Miyata et al., 2000), which also contains Phe in the proximal part of HP-helix Phe⁴⁷⁴). The lack of inhibition of myosin samples from the biopsies confirms that α -cardiac myosin could not be inhibited by MPH-220. We also note that gene products of *MYH1*, *MYH2* and *MYH4* encoding fast skeletal muscle myosin heavy chains IIX/d, IIA and IIB, respectively, are not expressed in adult human heart in significant amount ((England and Loughna, 2013), and NCBI Gene Expression database).**

In order to further analyze the molecular background of selectivity we crystallized fast skeletal muscle myosin (isolated from high-quality rabbit *m.psoas*) in the presence of MPH-220 (**Fig. 2A**, **Table S2**). The crystal structure confirmed that MPH-220 binds to the blebbistatin-binding cleft and its morpholine ring is in close proximity to Leu⁴⁷⁶. This residue is at the N-terminus of the so-called HP-helix of the L50 subdomain (Cope et al., 1996), which is preceded by the switch-2 loop and followed by the relay region of the motor. Comparison of the MPH-220-bound skeletal and blebbistatin-bound *Dictyostelium* myosin-2 structures confirms that while the tricyclic cores of the inhibitors including the chiral OH are positioned similarly, Phe⁴⁶⁶ of the HP-helix in *Dictyostelium* myosin-2 comes into steric hindrance with MPH-220 (**Fig. 2B**). Likewise, the position of this Phe in cardiac myosin structure also causes steric hindrance with MPH-220 (Planelles-Herrero et al., 2017) (**Fig. 2C**). This steric hindrance based on crystal structures together with the biochemical results strongly support that the unique Leu in the HP-helix of fast skeletal muscle myosin isoforms is responsible for the extreme selectivity of MPH-220. This mechanism for selective inhibition among myosin-2 isoforms is analogous to how blebbistatin is selective for myosin-2s due to the presence of the switch-2 Ser/Ala residue in myosin-2s (Allingham et al., 2005), while this position is occupied by Tyr/Phe in myosins from other classes that are uninhibited by blebbistatin. The resolved crystal structure also confirmed that MPH-220 selects and stabilizes the pre-powerstroke state. Overall, the structure validated the *in silico* approach to design molecules for selective inhibitor development (**Fig. S5**).

We further studied the effect of MPH-220 on muscle force generation in living animals (**Fig. 3A**). In agreement with the ATPase inhibitory properties (**Fig. S6**), the S(-) enantiomer of MPH-220 was drastically more effective than the R(+) enantiomer when animals were treated orally

with MPH-220 (**Fig. S7**). Consequently, the force-relaxing effect of the racemic mixture was significantly lower than that of the S(-) enantiomer. While the racemic mixture caused maximum 40% reduction, the S(-) enantiomer could decrease hindleg force by 70% in a concentration-dependent manner, (**Fig. 3B-C**). The 30% residual isometric force level for S(-)-MPH-220 is in line with the presence of uninhibitable slow skeletal muscle isoforms in rat hindleg muscles. This attribute is of high importance because unlike centrally acting muscle relaxants MPH-220 would never cause overdose related patient immobilization due to the remaining slow myosin-mediated muscle tone. Importantly, the decreased force persisted for more than 10 hours (**Fig. 3C**), which indicates optimal properties for pharmacological development. The force-relaxing effect after oral administration was only marginally slower than that after *intraperitoneal* injection (**Fig. S7**), which indicated optimal absorption properties of MPH-220. High endothelial permeability was further confirmed by Caco-2 assay, which showed that MPH-220 is highly permeable with significantly faster transfer rate in the absorptive direction over the excretive direction (**Fig. S7**).

While skeletal muscle relaxation could be efficiently achieved by MPH-220, cardiac function was not perturbed in the concentration range that was effective in skeletal muscle force relaxation experiments (**Fig. 3F**, **Fig. S8**). More importantly, neither cardiac nor respiratory functions differed significantly from the excipient control during the 10-hour experiments suggesting a reasonable safety range between the effective and toxic doses of MPH-220 (**Fig. 3E-F**). The maximum 25% decrease in heart rate and blood flow parameters is most probably due to the 10-hour-long anesthesia without food and drink after an overnight starvation period, and not the effect of myosin inhibition (**Fig. S8**). Moreover, the identical direction of the change in heart rate and blood flow parameters solely reflects slowing down the heart during anesthesia, because cardiac myosin inhibition preceding heart failure increases heart rate while drastically lowering blood flow as shown with the non-selective inhibitor, AmBleb (**Fig. S8**).

We also examined MPH-220 distribution in rat tissues in a time-dependent manner and observed a dose-dependent, few-fold accumulation of MPH-220 in skeletal muscle samples over other tissues including brain, heart, kidney and blood (**Fig. 3J-L**). Accumulation in skeletal muscle persists after 3 hours when MPH-220 is completely eliminated from blood and other tissues, while its concentration in target muscles is still in the effective concentration range (10-fold higher than the determined IC_{50}). MPH-220 concentration was only temporarily elevated in the liver, which metabolizes MPH-220. We note that MPH-220 concentration in the diaphragm was much lower compared to other striated muscle samples, which explains the lack of respiratory dysfunctions after MPH-220 treatments. This feature is expected to prove even more favorable in human patients due to the substantially higher ratio of MyHC I slow isoforms in human diaphragm (**Fig. S4**). The pronounced accumulation of MPH-220 in skeletal muscles might be the result of high concentration of fast skeletal myosin isoforms, which bind the inhibitor with high affinity. This hypothesis is supported by the significantly lower accumulation of the R(+) enantiomer (**Fig. S9**), which – besides its weaker inhibitory efficacy (**Fig. S6**) – further explains the fourfold weaker force relaxation by the R(+) enantiomer (cf. **Fig. 3B**). The species-specific MyHC distribution (**Fig. S4**) also emphasizes the need for testing these pharmacodynamic

properties of MPH-220 in larger animals (dogs, mini pigs), which – unlike rodents – have higher slow isoform proportions, more similar to human tissues.

Direct and efficient targeting of skeletal muscle contraction by MPH-220 raises the possibility of the development of a new generation nervous system-independent anti-spastic drug. Therefore, we investigated the efficiency of MPH-220 to improve spasticity-related gait disorders in rats with brain injury. We applied the recently developed spastic cerebral palsy animal model to provoke paralysis-coupled spasticity in rats (**Fig. 4A**) (Yu et al., 2013), and gait disorders were analyzed by non-invasive methods focusing on the motoric functions of rats combined with neural network based deep learning movement analysis (**Fig. 4B**, **Movie S1**). Similarly to human patients with stroke or brain trauma, rats showed individually variable gait patterns with different degrees of palsy in the lower limbs. Thus, we analyzed the effect of MPH-220 treatment individually on each animal and focused on treatment-induced changes in spasticity-related gait components.

Rat-A could not use the right forelimb and the left hindleg due to paralysis-coupled spasticity, which resulted in an almost complete one-sided circling behaviour in the open-field box two days after the surgery (**Movie S2**). 40 minutes after MPH-220 treatment the ratio of left turns increased from 15% to 38%, which further improved to 51% three hours after the treatment (**Fig. 4C**). Even though Rat-A walked significantly less after treatment, it was obvious that a major improvement was achieved: after relaxing spasticity in its left hindleg Rat-A was able to use this leg and make quasi-normal steps (**Movie S3**). Rat-B and C also had paralysis-coupled spasticity in the hindlegs, although, to a lower degree than Rat-A. The most obvious spasticity-related feature in the open field test was the random falling (**Movie S4**) and the spontaneous cramping of the right hindleg of Rat-C (**Movie S5**). Importantly, the relative frequency of both symptoms decreased drastically after MPH-220 treatment (**Fig. 4D**). Besides these serious gait abnormalities, Rat-B and C could not stand up in the cylinder assay before MPH-220 treatment. In agreement with the kinetics observed in the open field assay, three and five hours after oral MPH-220 treatment both rats could stand up in the cylinder touching the wall with both forepaws with the same number of events as their healthy littermates (**Fig. 4D**, **Fig. S10**). Next morning, the positive effects on falling and cramping frequencies, and on the ability to stand up in the cylinder disappeared as MPH-220 was excreted from their bodies. Rat-D showed spastic gait disorders only in the right hindleg without signs of severe palsy, while all other legs remained unaffected. This animal could not use the right hindleg normally due to stiff muscles, which resulted in abnormal positioning of all four paws (**Fig. 4E**, **Fig. S11**). The spastic leg was offset from the body axis, which hindered normal progression of the limb during walking, and resulted in lopsided gait patterns with tilted body axis (**Fig. 4F**, **Fig. S11**, **Movie S6**). After MPH-220 treatment the gait of this animal improved significantly as it started to use both hindlegs normally. The improved movement was the consequence of relaxed spasticity in the hindlegs, which enabled the animal to pull its leg into the body-axis thereby making normal walking steps (**Fig. 4E-F**, **Fig. S11**, **Movie S6**). The enhanced gait functions remained persistent for five hours, when paw positions and body symmetry was close to those of the healthy animals. Similarly to the other experiments, the effect relapsed to the pretreatment state after 21 hours.

These effects could be reproduced five and twelve days after the first treatment corroborating the specific anti-spastic effect of MPH-220 treatment.

Beside the individual patterns of spastic behavior that could be improved by MPH-220 treatment, deep learning analysis was used to assess the over-ground locomotion of all animals during 15 minutes of free movement in the open field test. We used 28 parameters characterizing the 3D position of the limbs and body axis in three movement speed regimes (**Table S3**) to quantify the locomotor features based on pose-estimating deep learning algorithms and exposed these to a principal components analysis (PCA). In the global PCA space – including all three speed-regimes – the major gait component (PC1) was significantly different from the healthy range, indicating that pyramidal tract damage-induced spastic walk asymmetry is reflected in the major principal gait component (**Fig. 5A**). Most importantly, MPH-220 treatment significantly decreased PC1 scores, the effect of which was maximal at 3 hours and no longer detected after 21 hours. Importantly, while PC1 scores were significantly different from the untreated level, the treated values did not differ significantly from the healthy range, which confirms that MPH-220 ameliorated gait pattern of the treated animals to that of the healthy rats. However, when we analyzed the three speed-regimes separately, we found that pyramid tract damage mostly affected PC1 in the slow and medium-speed regimes, while PC2 and PC3 were significantly affected in the fast regime (**Fig. 5B, Fig. S11**). More importantly, PC1 could be significantly improved by MPH-220 treatment in the slow and medium-speed regimes, while PC3 was significantly improved in the fast regime. We identified the major parameters that predominantly contributed to PC1 and PC3 in the slow, medium and fast regimes, and found a marked difference in the parameter sets defining PC1 and PC3 (**Fig. 5C-D, Fig. S11, Table S3**). Analysis of these components revealed that in the slow and medium-speed regimes MPH-220 treatment has the largest effect on the volumes of the ellipsoids representing paw positions and on the distances between their centers, both suggesting a much ordered stepping pattern and straightened body axis (**Fig. 5E**). On the other hand, in the fast regime, MPH-220 has the most pronounced effect on the angles of the ellipsoids, which indicates that the treated rats could keep their legs closer to the body axis similarly to the healthy running pattern. These results further solidify that MPH-220 is capable of treating the spastic component of movement abnormalities after brain injury, exhibiting a promising potential to address the unmet medical need for effective anti-spastic therapies.

Discussion

Our biochemical and *in vivo* results demonstrate that MPH-220 selectively inhibits fast skeletal myosin-2 isoforms, which enables effective improvements of spastic gait disorders after brain damage as a consequence of efficient reduction of muscle force. These findings emphasize that nervous system injury-derived muscle spasticity can be treated by directly targeting the effector protein of muscle contraction, thereby avoiding adverse neurological and cardiovascular side effects that are characteristic of currently used muscle relaxants. Moreover, as MPH-220 proved a promising candidate for further anti-spastic drug development, we tested its pharmacological

properties by investigating its off-target effects on human enzymes including kinase panels, G-protein coupled and nuclear hormone receptors (**Fig. S12**). We also demonstrate that MPH-220 is not mutagenic and not cytotoxic (**Fig. S12-13**) which, together with its high-absorption properties, confirm that MPH-220 is safe and possesses optimal attributes for further drug development as a new-generation anti-spastic drug candidate.

Although we acknowledge that MPH-220 may cause general muscle weakness as observed in our animal disease model. We believe that this effect will be significantly less pronounced in human patients due to the higher ratio of MyHC I slow skeletal muscle myosin isoform. In human skeletal muscles the presence of 40-60% MyHC I isoform, which is not inhibited by MPH-220, highlights another important aspect of this type of muscle relaxation as opposed to nervous system targeting medications. Although general weakness of aspecific muscle groups may appear by using both types of muscle relaxants, the MPH-220 based anti-spastic effect will never cause complete immobilization of patients due to the residual muscle tone from the uninhibited slow isoform fraction. Another concern may arise regarding extraocular muscles, which express MYH13 gene product containing Leu required for MPH-220 inhibition (**Fig. S1**). Nevertheless, in adult human extraocular muscles significant amount of α -cardiac myosin heavy chain is expressed (Kjellgren et al., 2003), therefore, these muscles will also not be completely immobilized by MPH-220. However, these effects might be investigated during future clinical trials.

Moreover, based on the complex pathophysiology of spasticity development (Trompetto et al., 2014) we suppose that early treatment with an effective anti-spastic drug will significantly delay the onset and markedly reduce the severity of spastic symptoms after nervous system injuries.

Beside traumatic brain and spinal cord injuries in stroke and cerebral palsy, spasticity is also a common symptom in several other diseases of broad etiology (**Table 1**). Spasticity is a major component of upper motor neuron lesion syndromes including multiple sclerosis, amyotrophic lateral sclerosis, spastic paraplegia, multiple system atrophy and atypical Parkinsonism, and also a characteristic symptom in several skeletal muscle myopathies such as myotonia congenita, myotonia fluctuans, or certain neurodegenerative diseases. Altogether, spasticity in these syndromes affect nearly 1% of the human population (cca. 55 million spastic patients) and more than 10% of people suffers from often-painful muscle stiffness in low back pain and fibromyalgia (Marques et al., 2017; Vos et al., 2012). Consequently, a nervous system-independent, safe and effective treatment is a significant unmet need from both clinical and socio-economical perspectives. Therefore MPH-220 is a promising anti-spastic drug candidate to improve quality of life and may contribute to extended life expectancy (Blair et al., 2019; Gillard et al., 2015; Slaman et al., 2014; Yi et al., 2019) of these patients and would provide new therapeutic protocols for clinicians in these diverse indications.

References:

Allingham, J.S., Smith, R., and Rayment, I. (2005). The structural basis of blebbistatin inhibition and specificity for myosin II. *Nat Struct Mol Biol* 12, 378-379.

Berman, H., Henrick, K., and Nakamura, H. (2003). Announcing the worldwide Protein Data Bank. *Nat Struct Biol* 10, 980.

- Billington, N., Wang, A., Mao, J., Adelstein, R.S., and Sellers, J.R. (2013). Characterization of three full-length human nonmuscle myosin II paralogs. *J Biol Chem* 288, 33398-33410.
- Bjornsdottir, A., Gudmundsson, G., Blondal, H., and Olafsson, E. (2013). Incidence and prevalence of multiple system atrophy: a nationwide study in Iceland. *Journal of neurology, neurosurgery, and psychiatry* 84, 136-140.
- Blair, E., Langdon, K., McIntyre, S., Lawrence, D., and Watson, L. (2019). Survival and mortality in cerebral palsy: observations to the sixth decade from a data linkage study of a total population register and National Death Index. *BMC neurology* 19, 111.
- Bose, P., Hou, J., and Thompson, F.J. (2015). Traumatic Brain Injury (TBI)-Induced Spasticity: Neurobiology, Treatment, and Rehabilitation. In *Brain Neurotrauma: Molecular, Neuropsychological, and Rehabilitation Aspects*, F.H. Kobeissy, ed. (Boca Raton (FL)).
- Bricogne, G., Blanc, E., Brandl, M., Flensburg, C., Keller, P., Paciorek, W., Roversi, P., Sharff, A., Smart, O.S., Vornrhein, C., *et al.* (2017). BUSTER version 2.10.3. (Cambridge, United Kingdom: Global Phasing Ltd.).
- Careta, M.F., Delgado, L., and Patriota, R. (2015). Report of Allergic Reaction After Application of Botulinum Toxin. *Aesthetic surgery journal* 35, NP102-105.
- Coluccio, L.M. (2020). Myosins and Disease. *Advances in experimental medicine and biology* 1239, 245-316.
- Cope, M.J., Whisstock, J., Rayment, I., and Kendrick-Jones, J. (1996). Conservation within the myosin motor domain: implications for structure and function. *Structure* 4, 969-987.
- Dewan, M.C., Rattani, A., Gupta, S., Baticulon, R.E., Hung, Y.C., Punchak, M., Agrawal, A., Adeleye, A.O., Shrime, M.G., Rubiano, A.M., *et al.* (2018). Estimating the global incidence of traumatic brain injury. *Journal of neurosurgery*, 1-18.
- Emsley, P., and Cowtan, K. (2004). Coot: model-building tools for molecular graphics. *Acta crystallographica Section D, Biological crystallography* 60, 2126-2132.
- England, J., and Loughna, S. (2013). Heavy and light roles: myosin in the morphogenesis of the heart. *Cellular and molecular life sciences : CMLS* 70, 1221-1239.
- Enslin, J.M.N., Rohlwink, U.K., and Figaji, A. (2020). Management of Spasticity After Traumatic Brain Injury in Children. *Frontiers in neurology* 11, 126.
- Gillard, P.J., Sucharew, H., Kleindorfer, D., Belagaje, S., Varon, S., Alwell, K., Moomaw, C.J., Woo, D., Khatri, P., Flaherty, M.L., *et al.* (2015). The negative impact of spasticity on the health-related quality of life of stroke survivors: a longitudinal cohort study. *Health and quality of life outcomes* 13, 159.
- Gotoh, T., Miyazaki, Y., Sato, W., Kikuchi, K., and Bentley, W.E. (2001). Proteolytic activity and recombinant protein production in virus-infected Sf-9 insect cell cultures supplemented with carboxyl and cysteine protease inhibitors. *Journal of bioscience and bioengineering* 92, 248-255.
- Gourinath, S., Himmel, D.M., Brown, J.H., Reshetnikova, L., Szent-Gyorgyi, A.G., and Cohen, C. (2003). Crystal structure of scallop Myosin s1 in the pre-power stroke state to 2.6 a resolution: flexibility and function in the head. *Structure* 11, 1621-1627.

- Gyimesi, M., Kintses, B., Bodor, A., Perczel, A., Fischer, S., Bagshaw, C.R., and Malnasi-Csizmadia, A. (2008). The mechanism of the reverse recovery step, phosphate release, and actin activation of Dictyostelium myosin II. *J Biol Chem* 283, 8153-8163.
- Heissler, S.M., and Manstein, D.J. (2011). Comparative kinetic and functional characterization of the motor domains of human nonmuscle myosin-2C isoforms. *J Biol Chem* 286, 21191-21202.
- Kawana, M., Sarkar, S.S., Sutton, S., Ruppel, K.M., and Spudich, J.A. (2017). Biophysical properties of human beta-cardiac myosin with converter mutations that cause hypertrophic cardiomyopathy. *Science advances* 3, e1601959.
- Kim, A.S., Cahill, E., and Cheng, N.T. (2015). Global Stroke Belt: Geographic Variation in Stroke Burden Worldwide. *Stroke* 46, 3564-3570.
- Kjellgren, D., Thornell, L.E., Andersen, J., and Pedrosa-Domellof, F. (2003). Myosin heavy chain isoforms in human extraocular muscles. *Investigative ophthalmology & visual science* 44, 1419-1425.
- Kovacs, M., Toth, J., Hetenyi, C., Malnasi-Csizmadia, A., and Sellers, J.R. (2004). Mechanism of blebbistatin inhibition of myosin II. *J Biol Chem* 279, 35557-35563.
- Kovacs, M., Wang, F., Hu, A., Zhang, Y., and Sellers, J.R. (2003). Functional divergence of human cytoplasmic myosin II: kinetic characterization of the non-muscle IIA isoform. *J Biol Chem* 278, 38132-38140.
- Kruse, M., Michelsen, S.I., Flachs, E.M., Bronnum-Hansen, H., Madsen, M., and Uldall, P. (2009). Lifetime costs of cerebral palsy. *Developmental medicine and child neurology* 51, 622-628.
- Laskowski, R.A., and Swindells, M.B. (2011). LigPlot+: multiple ligand-protein interaction diagrams for drug discovery. *Journal of chemical information and modeling* 51, 2778-2786.
- Li, S. (2017). Spasticity, Motor Recovery, and Neural Plasticity after Stroke. *Frontiers in neurology* 8, 120.
- Limouze, J., Straight, A.F., Mitchison, T., and Sellers, J.R. (2004). Specificity of blebbistatin, an inhibitor of myosin II. *J Muscle Res Cell Motil* 25, 337-341.
- Lundstrom, E., Terent, A., and Borg, J. (2008). Prevalence of disabling spasticity 1 year after first-ever stroke. *European journal of neurology* 15, 533-539.
- Maier, J.A., Martinez, C., Kasavajhala, K., Wickstrom, L., Hauser, K.E., and Simmerling, C. (2015). ff14SB: Improving the Accuracy of Protein Side Chain and Backbone Parameters from ff99SB. *Journal of chemical theory and computation* 11, 3696-3713.
- Malnasi-Csizmadia, A., and Kovacs, M. (2010). Emerging complex pathways of the actomyosin powerstroke. *Trends Biochem Sci* 35, 684-690.
- Margossian, S.S., and Lowey, S. (1982). Preparation of myosin and its subfragments from rabbit skeletal muscle. *Methods Enzymol* 85 Pt B, 55-71.
- Marques, A.P., Santo, A., Berssaneti, A.A., Matsutani, L.A., and Yuan, S.L.K. (2017). Prevalence of fibromyalgia: literature review update. *Revista brasileira de reumatologia* 57, 356-363.

- Martin, A., Abogunrin, S., Kurth, H., and Dinet, J. (2014). Epidemiological, humanistic, and economic burden of illness of lower limb spasticity in adults: a systematic review. *Neuropsychiatric disease and treatment* *10*, 111-122.
- Mathis, A., Mamidanna, P., Cury, K.M., Abe, T., Murthy, V.N., Mathis, M.W., and Bethge, M. (2018). DeepLabCut: markerless pose estimation of user-defined body parts with deep learning. *Nature neuroscience* *21*, 1281-1289.
- McCoy, A.J., Grosse-Kunstleve, R.W., Adams, P.D., Winn, M.D., Storoni, L.C., and Read, R.J. (2007). Phaser crystallographic software. *Journal of applied crystallography* *40*, 658-674.
- Medical Advisory, S. (2005). Intrathecal baclofen pump for spasticity: an evidence-based analysis. *Ontario health technology assessment series* *5*, 1-93.
- Meleger, A.L. (2006). Muscle relaxants and antispasticity agents. *Physical medicine and rehabilitation clinics of North America* *17*, 401-413.
- Meyer, T., Funke, A., Munch, C., Kettemann, D., Maier, A., Walter, B., Thomas, A., and Spittel, S. (2019). Real world experience of patients with amyotrophic lateral sclerosis (ALS) in the treatment of spasticity using tetrahydrocannabinol:cannabidiol (THC:CBD). *BMC neurology* *19*, 222.
- Miyata, S., Minobe, W., Bristow, M.R., and Leinwand, L.A. (2000). Myosin heavy chain isoform expression in the failing and nonfailing human heart. *Circulation research* *86*, 386-390.
- Mukherjee, A., and Chakravarty, A. (2010). Spasticity mechanisms - for the clinician. *Frontiers in neurology* *1*, 149.
- Nath, T., Mathis, A., Chen, A.C., Patel, A., Bethge, M., and Mathis, M.W. (2019). Using DeepLabCut for 3D markerless pose estimation across species and behaviors. *Nature protocols* *14*, 2152-2176.
- NIH, N.L.o.M. (2012). Dantrolene. In *LiverTox: Clinical and Research Information on Drug-Induced Liver Injury* (Bethesda (MD)).
- Novak, I. (2014). Evidence-based diagnosis, health care, and rehabilitation for children with cerebral palsy. *Journal of child neurology* *29*, 1141-1156.
- Opheim, A., Danielsson, A., Alt Murphy, M., Persson, H.C., and Sunnerhagen, K.S. (2014). Upper-limb spasticity during the first year after stroke: stroke arm longitudinal study at the University of Gothenburg. *American journal of physical medicine & rehabilitation* *93*, 884-896.
- Orsnes, G.B., Sorensen, P.S., Larsen, T.K., and Ravnborg, M. (2000). Effect of baclofen on gait in spastic MS patients. *Acta neurologica Scandinavica* *101*, 244-248.
- Pavone, V., Testa, G., Restivo, D.A., Cannavo, L., Condorelli, G., Portinaro, N.M., and Sessa, G. (2016). Botulinum Toxin Treatment for Limb Spasticity in Childhood Cerebral Palsy. *Frontiers in pharmacology* *7*, 29.
- Paxinos, G., and Watson, C. (2007). *The rat brain in stereotaxic coordinates*, 6th edn (Amsterdam ; Boston ;: Academic Press/Elsevier).
- Planelles-Herrero, V.J., Hartman, J.J., Robert-Paganin, J., Malik, F.I., and Houdusse, A. (2017). Mechanistic and structural basis for activation of cardiac myosin force production by omecamtiv mecarbil. *Nature communications* *8*, 190.

- Pollard, C.E., Abi Gerges, N., Bridgland-Taylor, M.H., Easter, A., Hammond, T.G., and Valentin, J.P. (2010). An introduction to QT interval prolongation and non-clinical approaches to assessing and reducing risk. *British journal of pharmacology* 159, 12-21.
- Pratt, S.J.P., and Lovering, R.M. (2014). A stepwise procedure to test contractility and susceptibility to injury for the rodent quadriceps muscle. *Journal of biological methods* 1.
- Pulgar, S., Bains, S., Gooch, J., Chambers, H., Noritz, G.H., Wright, E., Sawhney, T.G., Pyenson, B., and Ferro, C. (2019). Prevalence, Patterns, and Cost of Care for Children with Cerebral Palsy Enrolled in Medicaid Managed Care. *Journal of managed care & specialty pharmacy* 25, 817-822.
- Romitti, P.A., Zhu, Y., Puzhankara, S., James, K.A., Nabukera, S.K., Zamba, G.K., Ciafaloni, E., Cunniff, C., Druschel, C.M., Mathews, K.D., *et al.* (2015). Prevalence of Duchenne and Becker muscular dystrophies in the United States. *Pediatrics* 135, 513-521.
- Rychlik, R., Kreimendahl, F., Schnur, N., Lambert-Baumann, J., and Dressler, D. (2016). Quality of life and costs of spasticity treatment in German stroke patients. *Health economics review* 6, 27.
- Seidel, J.C. (1980). Fragmentation of gizzard myosin by alpha-chymotrypsin and papain, the effects on ATPase activity, and the interaction with actin. *J Biol Chem* 255, 4355-4361.
- Slaman, J., Roebroek, M., van der Slot, W., Twisk, J., Wensink, A., Stam, H., van den Berg-Emons, R., and Group, L.M.R. (2014). Can a lifestyle intervention improve physical fitness in adolescents and young adults with spastic cerebral palsy? A randomized controlled trial. *Archives of physical medicine and rehabilitation* 95, 1646-1655.
- Smit, C.A., and Slim, E.J. (2008). Heart conduction problems in a tetraplegic patient caused by a single therapeutic dosage of Baclofen. *Spinal cord* 46, 317-318.
- Sommese, R.F., Sung, J., Nag, S., Sutton, S., Deacon, J.C., Choe, E., Leinwand, L.A., Ruppel, K., and Spudich, J.A. (2013). Molecular consequences of the R453C hypertrophic cardiomyopathy mutation on human beta-cardiac myosin motor function. *Proc Natl Acad Sci U S A* 110, 12607-12612.
- Spudich, J.A., and Watt, S. (1971). The regulation of rabbit skeletal muscle contraction. I. Biochemical studies of the interaction of the tropomyosin-troponin complex with actin and the proteolytic fragments of myosin. *J Biol Chem* 246, 4866-4871.
- Straight, A.F., Cheung, A., Limouze, J., Chen, I., Westwood, N.J., Sellers, J.R., and Mitchison, T.J. (2003). Dissecting temporal and spatial control of cytokinesis with a myosin II Inhibitor. *Science* 299, 1743-1747.
- Sweeney, H.L., and Hammers, D.W. (2018). *Muscle Contraction. Cold Spring Harbor perspectives in biology* 10.
- Takacs, B., Billington, N., Gyimesi, M., Kintses, B., Malnasi-Csizmadia, A., Knight, P.J., and Kovacs, M. (2010). Myosin complexed with ADP and blebbistatin reversibly adopts a conformation resembling the start point of the working stroke. *Proc Natl Acad Sci U S A* 107, 6799-6804.
- Tofferi, J.K., Jackson, J.L., and O'Malley, P.G. (2004). Treatment of fibromyalgia with cyclobenzaprine: A meta-analysis. *Arthritis and rheumatism* 51, 9-13.

- Tong, C.W., Stelzer, J.E., Greaser, M.L., Powers, P.A., and Moss, R.L. (2008). Acceleration of crossbridge kinetics by protein kinase A phosphorylation of cardiac myosin binding protein C modulates cardiac function. *Circulation research* *103*, 974-982.
- Trompetto, C., Marinelli, L., Mori, L., Pelosin, E., Curra, A., Molfetta, L., and Abbruzzese, G. (2014). Pathophysiology of spasticity: implications for neurorehabilitation. *BioMed research international* *2014*, 354906.
- Trybus, K.M. (2000). Biochemical studies of myosin. *Methods* *22*, 327-335.
- Urban, P.P., Wolf, T., Uebele, M., Marx, J.J., Vogt, T., Stoeter, P., Bauermann, T., Weibrich, C., Vucurevic, G.D., Schneider, A., *et al.* (2010). Occurrence and clinical predictors of spasticity after ischemic stroke. *Stroke* *41*, 2016-2020.
- Vagin, A., and Teplyakov, A. (2010). Molecular replacement with MOLREP. *Acta crystallographica Section D, Biological crystallography* *66*, 22-25.
- Van Naarden Braun, K., Doernberg, N., Schieve, L., Christensen, D., Goodman, A., and Yeargin-Allsopp, M. (2016). Birth Prevalence of Cerebral Palsy: A Population-Based Study. *Pediatrics* *137*.
- van Tulder, M.W., Touray, T., Furlan, A.D., Solway, S., and Bouter, L.M. (2003). Muscle relaxants for non-specific low back pain. *The Cochrane database of systematic reviews*, CD004252.
- Verplancke, D., Snape, S., Salisbury, C.F., Jones, P.W., and Ward, A.B. (2005). A randomized controlled trial of botulinum toxin on lower limb spasticity following acute acquired severe brain injury. *Clinical rehabilitation* *19*, 117-125.
- Vonrhein, C., Flensburg, C., Keller, P., Sharff, A., Smart, O., Paciorek, W., Womack, T., and Bricogne, G. (2011). Data processing and analysis with the autoPROC toolbox. *Acta crystallographica Section D, Biological crystallography* *67*, 293-302.
- Vos, T., Flaxman, A.D., Naghavi, M., Lozano, R., Michaud, C., Ezzati, M., Shibuya, K., Salomon, J.A., Abdalla, S., Aboyans, V., *et al.* (2012). Years lived with disability (YLDs) for 1160 sequelae of 289 diseases and injuries 1990-2010: a systematic analysis for the Global Burden of Disease Study 2010. *Lancet* *380*, 2163-2196.
- Wallin, M.T., Culpepper, W.J., Campbell, J.D., Nelson, L.M., Langer-Gould, A., Marrie, R.A., Cutter, G.R., Kaye, W.E., Wagner, L., Tremlett, H., *et al.* (2019). The prevalence of MS in the United States: A population-based estimate using health claims data. *Neurology* *92*, e1029-e1040.
- Wang, F., Kovacs, M., Hu, A., Limouze, J., Harvey, E.V., and Sellers, J.R. (2003). Kinetic mechanism of non-muscle myosin IIB: functional adaptations for tension generation and maintenance. *J Biol Chem* *278*, 27439-27448.
- Wang, J., Wolf, R.M., Caldwell, J.W., Kollman, P.A., and Case, D.A. (2004). Development and testing of a general amber force field. *Journal of computational chemistry* *25*, 1157-1174.
- Waterhouse, A., Bertoni, M., Bienert, S., Studer, G., Tauriello, G., Gumienny, R., Heer, F.T., de Beer, T.A.P., Rempfer, C., Bordoli, L., *et al.* (2018). SWISS-MODEL: homology modelling of protein structures and complexes. *Nucleic Acids Res* *46*, W296-W303.
- Wissel, J., Manack, A., and Brainin, M. (2013). Toward an epidemiology of poststroke spasticity. *Neurology* *80*, S13-19.

- Witiw, C.D., and Fehlings, M.G. (2015). Acute Spinal Cord Injury. *Journal of spinal disorders & techniques* 28, 202-210.
- Xu, L., Liu, T., Liu, L., Yao, X., Chen, L., Fan, D., Zhan, S., and Wang, S. (2019). Global variation in prevalence and incidence of amyotrophic lateral sclerosis: a systematic review and meta-analysis. *Journal of neurology*.
- Yi, X., Luo, H., Zhou, J., Yu, M., Chen, X., Tan, L., Wei, W., and Li, J. (2020). Prevalence of stroke and stroke related risk factors: a population based cross sectional survey in southwestern China. *BMC neurology* 20, 5.
- Yi, Y.G., Jung, S.H., and Bang, M.S. (2019). Emerging Issues in Cerebral Palsy Associated With Aging: A Psychiatrist Perspective. *Annals of rehabilitation medicine* 43, 241-249.
- Yu, Y., Li, L., Shao, X., Tian, F., and Sun, Q. (2013). Establishing a rat model of spastic cerebral palsy by targeted ethanol injection. *Neural regeneration research* 8, 3255-3262.
- Zhang, Y., Li, L., Zhao, Y., Han, H., Hu, Y., Liang, D., Yu, B., and Kou, J. (2017). The Myosin II Inhibitor, Blebbistatin, Ameliorates FeCl₃-induced Arterial Thrombosis via the GSK3beta-NF-kappaB Pathway. *International journal of biological sciences* 13, 630-639.
- Zorowitz, R.D., Gillard, P.J., and Brainin, M. (2013). Poststroke spasticity: sequelae and burden on stroke survivors and caregivers. *Neurology* 80, S45-52.

Acknowledgments: We would like to thank Prof. Árpád Dobolyi for help in rat operations; and Máté Winternitz, Noémi Karnok, Kinga Oravecz and Henrietta Hóf for technical assistance; and beam line scientists of PX2A (SOLEIL synchrotron) for excellent support during data collection. We also thank Prof. James R. Sellers (NIH-NHLBI) for detailed discussions and helpful comments on the manuscript; and Prof. Matthias Preller (MHH) for helpful discussions regarding MD simulations.

Funding: This study has been supported by the Hungarian National Research, Development and Innovation Office (NVKP 16-1-2016-0051 to MG, AÁR and AMC) and the Hungarian Ministry of Finance (GINOP-2.1.7-15-2016-02580 to MG and AÁR). LC is the recipient of a PhD fellowship from Ligue contre le cancer IP/SC-16058. AH was supported by grants from CNRS, FRM DCM20181039553, ANR-17-CE11-0029-01, AFM 21805. The AH team is part of the Labex CelTisPhyBio:11-LBX-0038, which is part of the IDEX PSL (ANR-10-IDEX-0001-02 PSL). DVT, KMR and JAS are supported by National Institutes of Health grants R01 GM033289 and R01 HL1171138. DVT is supported by an American Heart Association postdoctoral fellowship (17POST33411070).

Author contributions: MG: conceptualization, formal analysis, funding acquisition, investigation, methodology development, supervision, validation, visualization and writing, ÁIH: investigation, formal analysis, and validation, DT: investigation, software development, formal

analysis, and validation, SKS: investigation, formal analysis, MP: investigation, methodology development, CK: investigation, formal analysis, LC: investigation, methodology development, crystallization and structure determination, formal analysis, CK: investigation, methodology development, structure refinement and formal analysis, KMR: investigation, preparation of human cardiac myosin sample, DVT: investigation, preparation of human cardiac myosin sample, JAS: funding acquisition and supervision for human cardiac myosin sample, IL: investigation, methodology development, formal analysis, AÁR: funding acquisition, writing – review & editing, MK: funding acquisition, supervision, writing – review & editing, EP: investigation, SK: conceptualization, funding acquisition, AH: methodology development, formal analysis, funding acquisition for crystallization and structure determination, AMC: conceptualization, formal analysis, funding acquisition, investigation, methodology development, supervision, validation, visualization, writing

Declaration of Interests: The authors declare the following competing interests: Employment: AMC, MG are owners of Optopharma Ltd., AÁR and MG are part-time employed by Optopharma Ltd. Related patents: PCT/EP2017/051829, WO/2017/129782, HU1800129A2; PCT/HU2019/050017, WO/2019/202346A2, WO/2019/202346A3. JAS is a cofounder and member of the scientific advisory boards of Cytokinetics and MyoKardia, biotechnology companies developing small molecules that target the sarcomere for the treatment of various muscle diseases. KMR is on the scientific advisory board at MyoKardia. JAS, DVT and KMR are cofounders of Kainomyx Inc., a biotechnology company focused on developing small molecules to target tropical diseases.

Data availability:

The atomic model is available in the PDB (Berman et al., 2003) under PDB ID 6YSY.

Disease	Background	Symptom	Prevalence (per 100,000)	Patient number	Ratio of spasticity
Stroke	Blood flow disruption in the brain either by a blood clot or by hemorrhage	Weakness, paralysis, spasticity, coordination and balance problems, memory problems	100-600 (Kim et al., 2015; Yi et al., 2020)	30 million	38-46% (Lundstrom et al., 2008; Opheim et al., 2014; Urban et al., 2010; Wissel et al., 2013) (11-14 million spastic patients)
Multiple sclerosis (MS)	Autoimmune disease attacking the myelin sheaths of nerve fibers	Fatigue, gait difficulties, numbness, spasticity, weakness, vision problems	300-400 in US (Wallin et al., 2019)	2.3 million	50% ^a (1.5-2 million spastic patients)
Cerebral palsy (CP)	Brain development disorders or disruption, due to genetic mutations, infections, trauma or injury	Muscle stiffness, spasticity, ataxia, tremors, gait disorders	150-300 (Kruse et al., 2009; Pulgar et al., 2019; Van Naarden Braun et al., 2016)	17 million	70-75% (Novak, 2014; Pulgar et al., 2019) (12-13 million spastic patients)
Amyotrophic lateral sclerosis (ALS)	Degeneration of cortical motor neurons, the motor nuclei of the brainstem, and the anterior horn cells of the spinal cord	Muscle weakness, atrophy, spasticity	4-5 (Xu et al., 2019)	14-15,000 (US) ^b	40% (Meyer et al., 2019) (6,000 spastic patients)
Traumatic brain injury	Blow or jolt to the head or a head injury that disrupts normal functions	Paralysis, sensory impairments, headaches, coordination, spasticity	1% (up to 15%) (Dewan et al., 2018), 475,000 children/year (US) (Enslin et al., 2020)	1.7-2 million new TBI/year [§] in US (Enslin et al., 2020), 68-71 million worldwide (Dewan et al., 2018)	5-19% (Bose et al., 2015; Verplancke et al., 2005) (30-35 million spastic patients)
Multiple system atrophy (MSA)	Progressive neurodegenerative disease with alpha-synuclein accumulation in glia (form of atypical Parkinsonism)	Slow movement, muscle stiffness, spasticity, incoordination, tremors, bladder control problems	2-6 (Bjornsdottir et al., 2013)		
Spastic paraplegia	Defects in transport of proteins, lipids through long nerve fibers (axons).	Progressive gait disorder, spasticity	3-6		
Myotonia congenita (Becker disease)	Abnormality of skeletal muscle membranes resulting in hyperexcitability	Painless spasm, difficulty relaxing muscles (myotonia), rigidity, abnormally enlarged muscles (hypertrophy)	1-2 (Romitti et al., 2015)		
Spinal cord injury or tumors	Nerve damage due to e.g. thoracic spine herniated discs damage the nerves	Pain, increased reflexes in legs that can cause spasticity, muscle weakness, numbness or tingling	2-8 (Witiw and Fehlings, 2015)		

Table 1. Prevalence and economic burden of diseases with broad etiologies in which muscle spasticity is one of the major characteristic symptoms

^a WHO Atlas multiple sclerosis resources in the world 2008 (who.int/mental_health/neurology)

^b NIH Amyotrophic Lateral Sclerosis (ALS) brochure (ninds.nih.gov/Disorders)

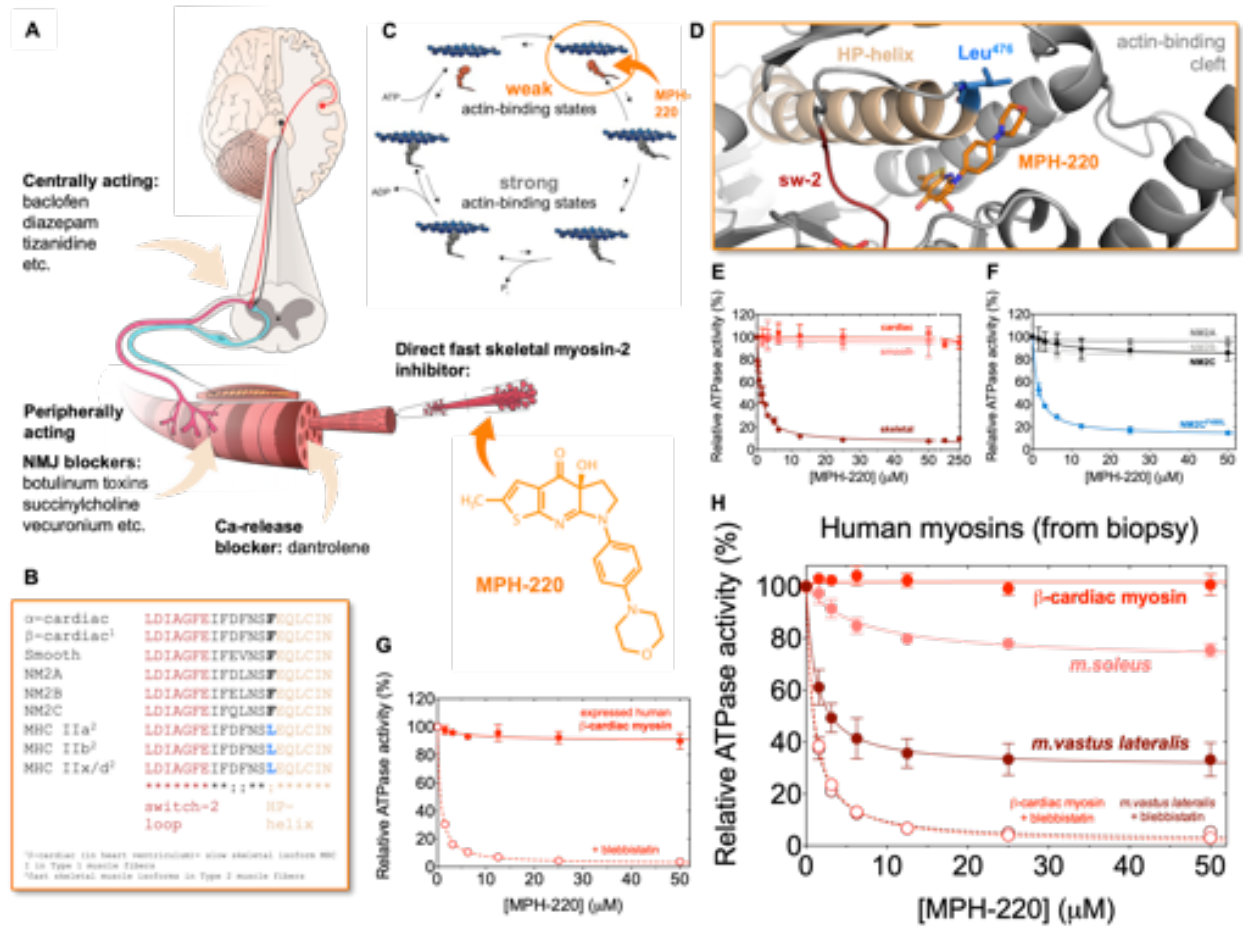


Figure 1. MPH-220 inhibits skeletal muscle myosin with extreme selectivity independently of the nervous system. (A) Current muscle relaxants target the central nervous system or act peripherally, while MPH-220 directly inhibits myosin. (B) Human myosin-2 isoforms contain phenylalanine (black F) at the beginning of the HP-helix between the switch-2 loop (red) and the relay region, except for fast skeletal myosin isoforms, where this position is leucine (blue L) (cf. **Fig. S1**). (C) MPH-220 was designed to bind into the blebbistatin-binding cavity of the motor domain, to enable inhibition in the actin-detached state. (D) Close-up view of the communication center of the functional regions (actin-binding cleft, switch-2 loop of the active site and the HP-relay-converter region) in the homology model of MyHC IIa with bound MPH-220 (orange) reveals interaction between the morpholino group and Leu⁴⁷⁶ in the HP-helix. (E) Actin-activated ATPase inhibition of six myosin-2 isoforms (cf. **Table S1**). (F) Actin-activated ATPase inhibition of NM2C and the NM2C^{F490L} variant. (G) Actin-activated ATPase inhibition of expressed human β -cardiac myosin with MPH-220 and blebbistatin. (H) Actin-activated ATPase inhibition of human muscle myosin samples from biopsies of *m. soleus*, *m. vastus lateralis* and heart ventricle. In contrast to MPH-220, blebbistatin fully inhibited *m. vastus lateralis* sample and β -cardiac myosin samples. Mean \pm SD is shown in all ATPase experiments, $n=3-9$.

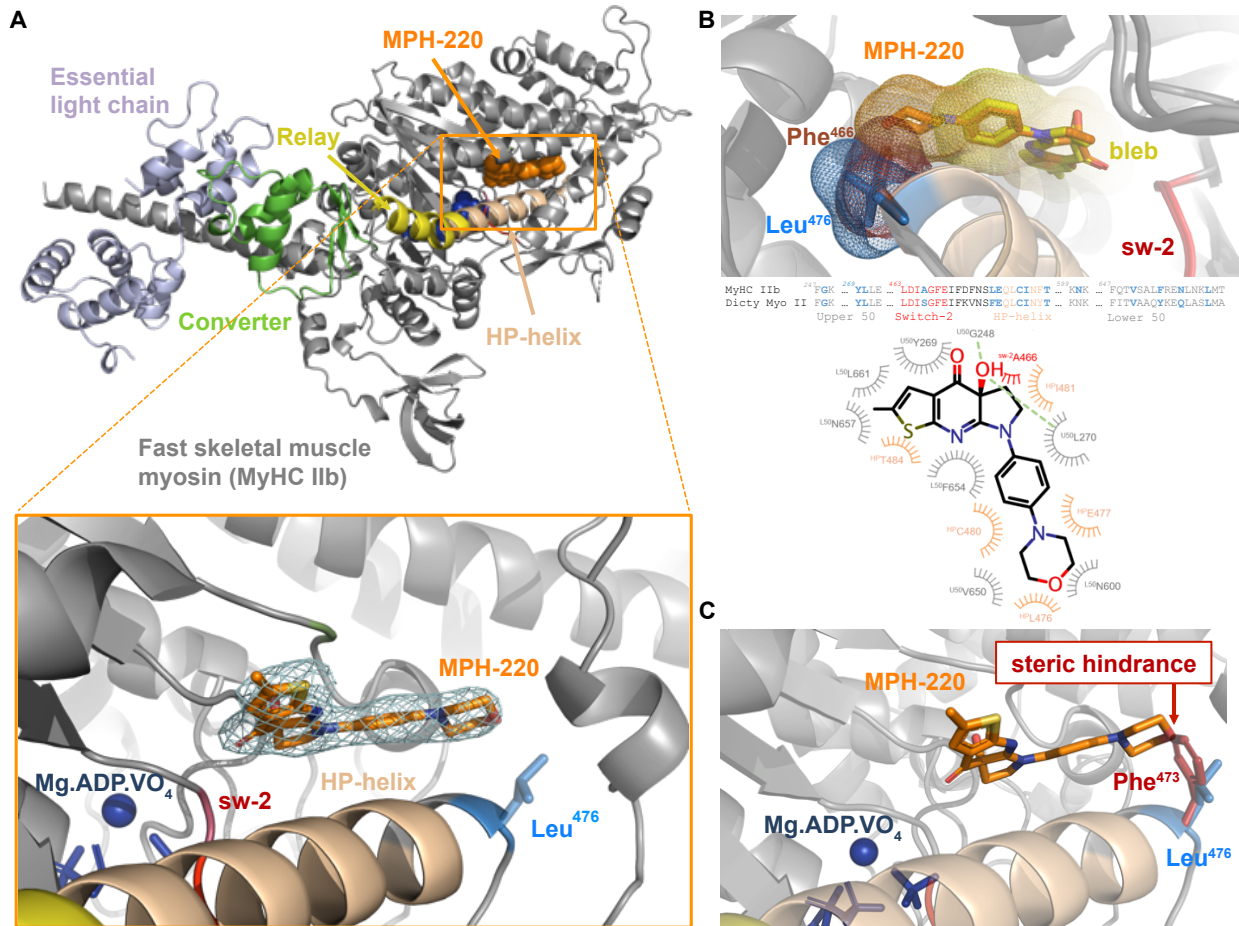


Fig. 2. Crystal structure of MPH-220-bound fast skeletal muscle myosin. (A) Cartoon representation of the heavy chain (gray) of rabbit skeletal muscle myosin-2 in Mg.ADP.VO₄ (spheres, blue) pre-power-stroke state with the essential light chain bound to the lever arm (Table S2). MPH-220 binds to the bottom of the actin-binding cleft close to the HP-helix, with its morpholine ring in close proximity of Leu⁴⁷⁶. Blue mesh: electron density corresponding to MPH-220 at sigma 1.0. (B) Comparison of the MPH-220 (orange) binding site in MyHC IIb (gray/beige) and the blebbistatin (yellow) binding site in *Dictyostelium* myosin-2 (dark gray/brown) (1YV3.pdb (Allingham et al., 2005)). The chiral OH groups of both inhibitors interact with the same residues Gly²⁴⁸ and Leu²⁷⁰ (Gly²⁴⁰ and Leu²⁶² in *Dictyostelium*). Mesh: surfaces based on Van-der-Walls radii, calculated with PyMol. (Bottom) Residues involved in compound binding in Ligplot+ v2.2 (Laskowski and Swindells, 2011) representation; U50: upper 50-kDa subdomain and L50: lower 50-kDa subdomain (gray); sw-2: switch-2 loop (red); HP: HP-helix (beige). Hydrogen bonds (up to 3.2 Å) are shown as green lines. (C) MPH-220 bound MyHC IIb structure with superimposed cardiac HP-helix illustrates the steric clash between the morpholine ring of MPH-220 and the cardiac HP-helix Phe⁴⁷³ (red) residue.

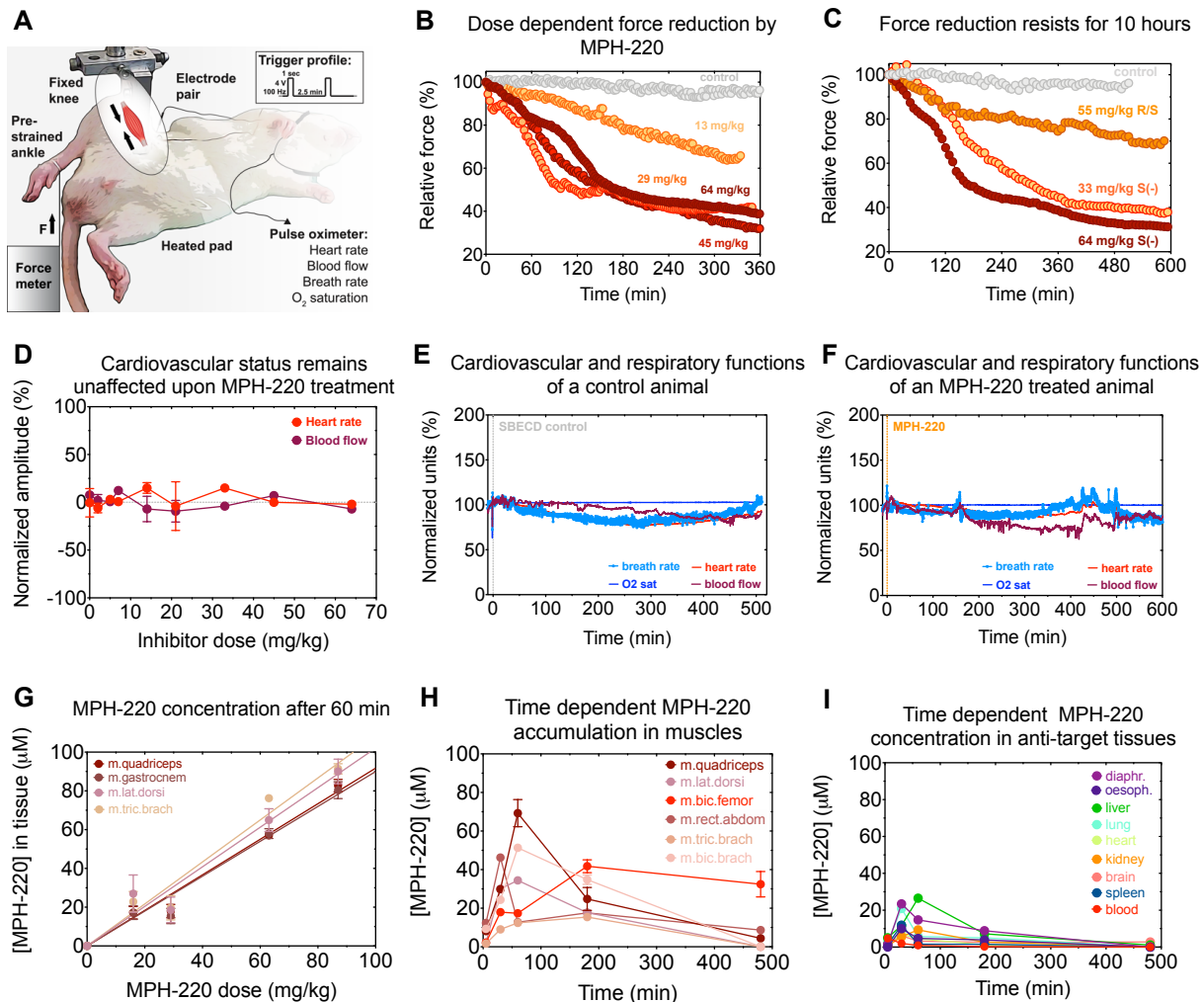


Fig. 3. MPH-220 reduces skeletal muscle force without cardiovascular effects. (A) Isometric force of rat hindleg was measured, while vital functions were detected by a non-invasive pulse oximeter. (B-C) Dose dependent force reduction after MPH-220 treatment persisted for more than 10 hours. (D) Heart rate (red circle) and pulse distention - reflecting local blood flow at the carotid artery - (maroon circle) show the maximal signal deflections during the measurements (60–600 min) on 1–4 animals/dose. (E-F) Cardiovascular and respiratory functions as a function of time after treatment with SBECD control or MPH-220. Note that permanent oxygen level is maintained by O₂-supplemented isoflurane anesthesia. (G) Dose-dependent MPH-220 accumulation in rat muscle tissues 60 minutes after oral treatment. (H-I) Time-dependent MPH-220 accumulation in rat tissues after 35 mg/kg *i.p.* treatment.

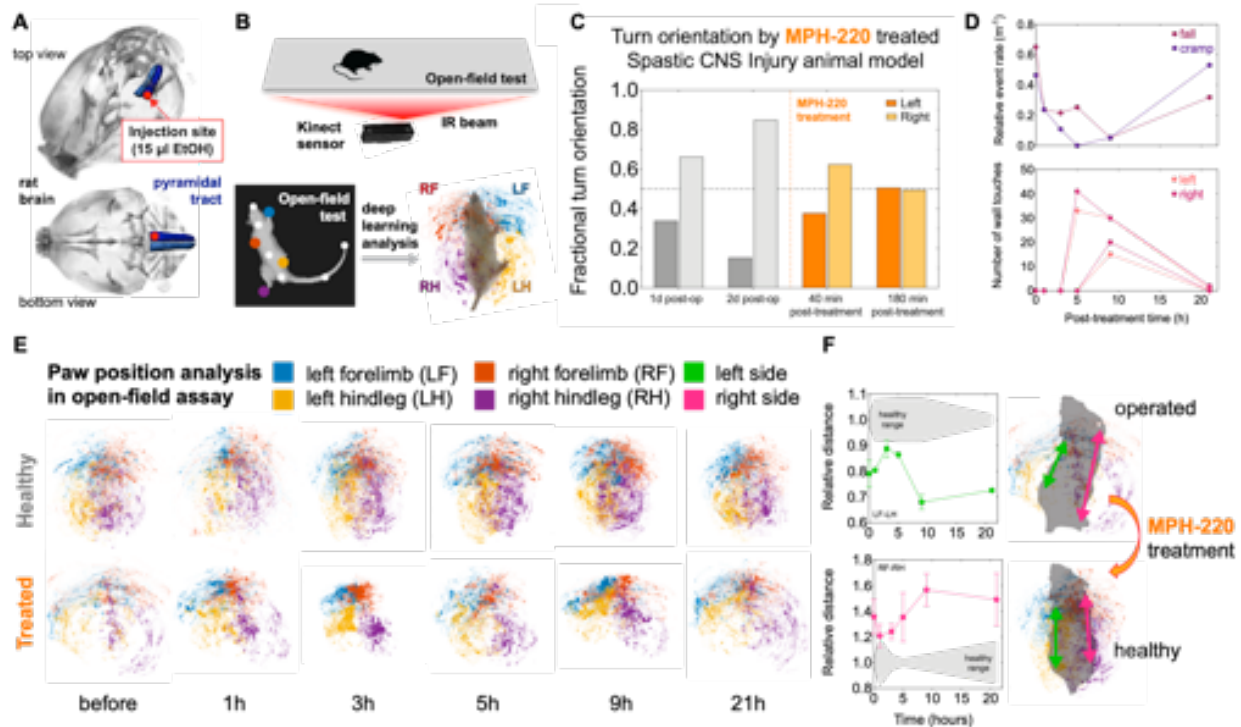


Fig. 4. MPH-220 efficiently improves gait functions of spastic rats after brain injury. (A) Position of pyramidal tract lesion (red dots). (B) Open-field gait analysis was performed by deep-learning algorithms coupled to sub-millimeter 3D movement detection. Dots represent the determined positions; right and left forelimbs (RF, LF), right and left hindlegs (RH, LH). (C) Fractional turn orientation of spastic rat before (gray) and after (orange) 15 mg/kg MPH-220 treatment. (D) Falling and spontaneous cramping rates normalized to the total distance travelled (*upper*) and the number of touches on the cylinder wall (*lower*) after 20 mg/kg MPH-220 treatment. (E) Paw position distribution of the healthy (*upper*) and treated (*lower*) animals before and after 20 mg/kg MPH-220 treatment in slow regime. (F) Averaged distances between the left (*upper*) and right (*lower*) fore- and hindlimbs in each frame of the 3D recordings relative to the healthy values.

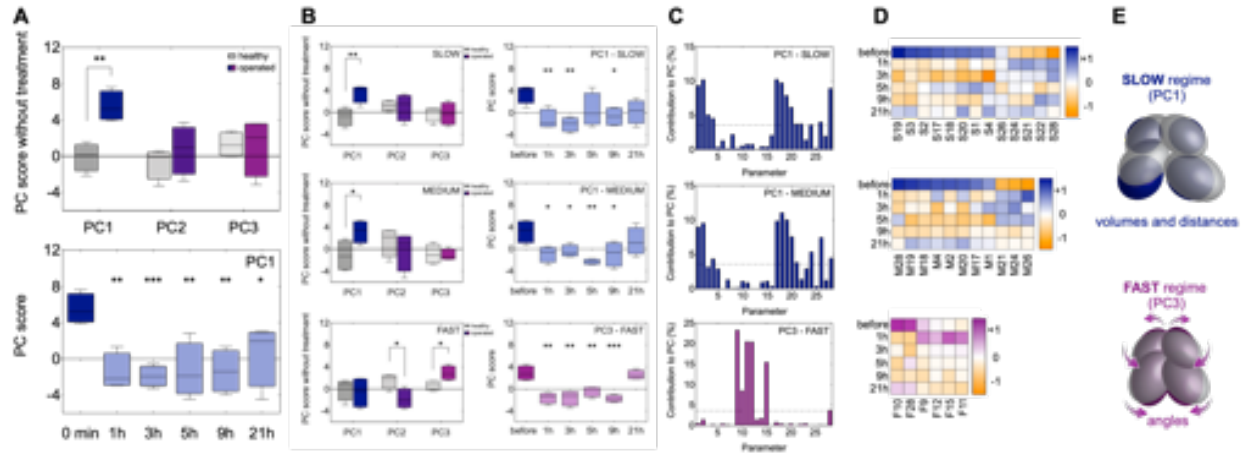


Fig. 5. Principal component analysis of spastic rats reveals details of improved gait components after MPH-220 treatment. Global (A) and speed-specific (B) principal component (PC) analysis of gait parameters of healthy (gray) and operated (colored) animals before (darker) and after (lighter) MPH-220 treatment. (C) Parameter contributions to PC1 in the slow and medium regimes and to PC3 in the fast regimes (cf. Table S3). (D) Heatmap of major parameters contributing to PC1 (blue-orange) and PC3 (purple-orange) (cf. Table S3). (E) Schematic representation of MPH-220 effects on paw positions in slow and fast regimes.

Supplemental Information for “Single residue variation in skeletal muscle myosin enables selective targeting: a small-molecule inhibitor ameliorates spastic gait disorder”

Máté Gyimesi, Ádám I. Horváth, Demeter Túrós, Sharad Kumar Suthar, Máté Péntzes, Csilla Kurdi, Louise Canon, Carlos Kikuti, Kathleen M. Ruppel, Darshan V. Trivedi, James A. Spudich, István Lőrincz, Anna Á. Rauscher, Mihály Kovács, Endre Pál, Sámuel Komoly, Anne Houdusse, András Málnási-Csizmadia*

STAR Methods

Resource availability

Lead Contact

Further information and requests for resources and reagents should be directed to and will be fulfilled by the Lead Contact, András Málnási-Csizmadia (malna@elte.hu)

Materials Availability

There are restrictions to the availability of MPH-inhibitors due to related patents: PCT/EP2017/051829, WO/2017/129782, HU1800129A2; PCT/HU2019/050017, WO/2019/202346A2, WO/2019/202346A3. Access to these materials should be required from Optopharma Ltd.

Data and Code Availability

The published article includes all datasets generated or analyzed during this study. The atomic model is available in the PDB under PDB ID 6YSY.

Method details

Materials

All chemicals were purchased from Sigma-Aldrich (Germany) if otherwise not stated. Sulphobutyl-ether- β -cyclodextrin (DexolveTM (SBECD)) was obtained from Cyclolab (Hungary). HPLC-grade acetonitrile, chloroform and water were purchased from VWR (PA, USA). Blebbistatin was purchased from Sellekchem (TX, USA), AmBleb and NBleb are products of Optopharma Ltd., and isoflurane was purchased from Rotacher-Medical GmbH

(Germany). Ames Microplate Format Mutagenicity Assay kit was purchased from Xenometrix (Switzerland).

Proteins

Rabbit actin was prepared as described previously from rabbit muscle acetone powder (Pel-Freez Biologicals Llc., AR, USA)(Spudich and Watt, 1971). Skeletal muscle myosin subfragment-1 (S1) was prepared from rabbit *m.psoas* according to an earlier published protocol (Margossian and Lowey, 1982) by α -chymotryptic digestion (0.25 mg/ml α -chymotrypsin, 10 min, 25°C; reaction was stopped with 3 mM PMSF). Psoas S1 prep was further purified on MonoS 5/50 GL column to produce high-quality prep for crystallization. Cardiac muscle myosin S1 was isolated from left ventricle of porcine heart following cardiac myofibril preparation protocol (Tong et al., 2008) by α -chymotryptic digestion (0.05 mg/ml α -chymotrypsin, 10 min, 25°C; reaction was stopped with 3 mM PMSF). Human cardiac muscle myosin subfragment-1 (S1) was prepared from adult human left ventricular tissue samples obtained from ethically consented donors (AnaBios Corporation) according to earlier published protocol (Margossian and Lowey, 1982) by α -chymotryptic digestion (0.25 mg/ml α -chymotrypsin, 9 min, 25°C; reaction was stopped with 3 mM PMSF). Smooth muscle myosin S1 was prepared from chicken gizzard (Trybus, 2000) by activated papain digestion (Seidel, 1980) (0.2 mg/ml papain, 12 min, 25°C; reaction was stopped with 5 mM sodium iodoacetate). Human skeletal muscle myosin was prepared similarly to rabbit skeletal muscle myosin (Margossian and Lowey, 1982). Briefly, biopsies were washed in Rigor Buffer (20 mM MOPS pH 7.4, 40 mM KCl, 2 mM MgCl₂) and myosin was extracted in Myosin Extraction Buffer (20 mM MOPS pH 7.4, 500 mM KCl). Extracted myosin was precipitated in 21-volume ultrapure water with 1 mM EDTA. Myosin was collected in tabletop centrifuge, dissolved in Myosin Extraction Buffer and kept on ice until the measurement. The Sf9 codon optimized sequences for NM2 motor domains (Met¹-Arg⁷⁷⁵ for NM2A, Met¹-Arg⁷⁸² for NM2B (B0) and Met¹-Arg⁷⁹⁹ for NM2C (C0)) fused to an Ala-Ser linker and an artificial α -actinin lever arm (as described earlier for NM2C (Heissler and Manstein, 2011)) with C-terminal FLAG-tag sequences were synthesized and cloned into pFastBac1 expression vector. The NM2C-F490L construct was also synthesized by Biomatik Co in pFastBac1 expression vector. The pFastBac1/NM2 constructs were overexpressed in Sf9 cells after bacmid preparation from DH10Bac cells. To reduce proteolytic digestion during expression, Pepstatin-A (0.1 mg/l) was added to Sf9 cells (Gotoh et al., 2001). Expressed human β -cardiac myosin S1 (Kawana et al., 2017) was prepared as earlier described (Sommese et al., 2013).

ATPase measurement

Steady-state ATPase measurements were carried out in 50 μ l volume in a flat bottom 384-well plate (Nunc-Thermo Fischer) using NADH-PK/LDH coupled assay described previously (Gyimesi et al., 2008) at 25°C in the presence of 0.5 mM ATP and 25 μ M F-actin in ATPase buffer (10 mM MOPS pH 7.0, 4 mM MgCl₂, 2 mM β -mercaptoethanol) for 15 minutes. ATPase

activity was calculated from linear regression of the time dependent absorbance data collected at 340 nm. Different concentrations of inhibitors were added to the reaction in 0.5 μ l DMSO (1% of total volume). DMSO and actin-controls were measured for each measurement set.

Animals

200-250 g male Wistar rats were obtained from Toxi-Coop (Hungary) or Animal Facility, Basic Medical Science Center at Semmelweis University (Hungary). Animals were maintained in standard housing conditions with 12-12-hour light-dark periods and were allowed free access to dry rat food and water. All procedures were conducted in accordance with the ARRIVE guidelines and the guidelines set by the European Communities Council Directive (86/609 EEC) and approved by the Animal Care and Use Committee of the Eötvös University (registration number: 48/1/2015) under the permission numbers: PE/EA/142-5/2020, PE/EA/143-7/2020.

Molecular dynamic simulation

Simulations were carried out using the AMBER16 program suite. The ff14SB force field (Maier et al., 2015) was used in all subsequent simulations to model protein interactions. The initial structure of the Fast Human Skeletal myosin-2 motor domain was modeled using structural homology with the SWISS-MODEL server (Waterhouse et al., 2018) using the Human Cardiac myosin-2 motor domain (PDB ID 5n69). ADP.VO₄ was substituted to ADP.PO₄. Coordinates and partials charges for MPH-220 were refined using *antechamber* of the AMBERTOOLS package with the AM1 semi-empirical Hamiltonian. Force field parameters for the MPH-220 atoms were adopted from GAFF force field (Wang et al., 2004) based on structural similarity following the suggestions of the *parmchk2* program. In order to determine the initial position of MPH-220 we RMSD least-square fitting the model's structure with the blebbistatin-*Dyctiostelium* motor domain (PDB ID 3bz9) binding pocket. The initial position was then determined by RMSD least-square fitting the tricyclic ring of MPH-220 to blebbistatin's tricyclic ring. The water molecules resolved by crystallography were retained and the model was expanded in an 8-Angstrom clearance dodecahedron box with TIP3P water molecules for explicit solvation and counterions were added to neutralize the system's net charge. The complex was minimized with 2000 steps steepest descent followed by 4000 steps of conjugate gradient method while applying 10 kcal/(mol Å²) to all atoms except water molecules. The minimization is continued with the same protocol while removing the restraint from all H atoms. The same restraints were applied for the following steps. The complex was heated in 3 100-K 20-ps steps to 300 K under NVT conditions, then subsequently equilibrated to 1 bar in 20 ps under NPT conditions. NPT conditions were applied in all further steps. The system was cooled back to 10 K in the next 20 ps. Restraints from this point were only applied to the protein backbone. The system was heated back to 300 K in 10 ps and the simulation was continued for 1ns. The restraint force was then gradually reduced in 1 ns simulations steps to 5, 1, 0.5 and 0 kcal/(mol Å²). The simulation was then allowed to continue and equilibrate under NPT conditions for a

further 200 ns to obtain the final structures. The trajectories were sampled every 50 ps during the simulation.

Crystallisation and data processing

MyCH IIB-MPH-220 crystals were obtained by vapor diffusion using a protein solution at 10 mg/ml containing 10 mM MOPS pH 7.3; 50 mM NaCl; 3 mM MgCl₂; 0.2 mM ATP; 3 mM NaN₃; 1 mM DTT; 0.1 mM EGTA; 0.1 mM PMSF; 1 µg/ml leupeptin, 2mM MgADP, 2mM VO₄, 0.5 mM MPH-220 against a reservoir containing 35% PEG600, 20mM DTT; 100mM HEPES pH 7.0; 5% DMSO at 291K. Optimization of crystallization conditions was performed with trypsin *in situ* proteolysis. Crystals were frozen then shot in the Proxima2 beamline (synchrotron Soleil). X-ray diffraction images were processed with AutoProc (Vonrhein et al., 2011). The crystal belongs to the P2₁2₁2₁ space group with one molecule per asymmetric unit. The data collection and refinement statistics are presented in (**Table S2**).

Structure determination and refinement

Structure of the motor domain was initially solved by molecular replacement using 1QVI (Gourinath et al., 2003) as a search model in Molrep (Vagin and Teplyakov, 2010), and completed with a second search for the lever arm and its essential light chain from 5N69 (Planelles-Herrero et al., 2017) with Phaser (McCoy et al., 2007). Refinement constraints for the ligand were automatically generated with Grade (Bricogne et al., 2017). The final model was obtained after several cycles of building in Coot (Emsley and Cowtan, 2004) and refinement with the latest 2019 release of BUSTER-TNT (Bricogne et al., 2017).

Isometric force measurement

Isometric force of rat left hindleg was measured by a force meter (Supertech Ltd.) after the hindleg was fixed and stimulated according to earlier published protocol (Pratt and Lovering, 2014). A non-elastic wire was attached to the ankle of the rat and pulled until pre-strained position. Spike^(R) software controlled stimulator (BioStim, Supertech Ltd.) was used to trigger the *n. femoralis* through metal electrodes with 100 Hz, 1 sec, 4V, 2.5 minute intervals. Data detection was performed with CED Micro 1401 data acquisition interface. Inhibitors were either dissolved in 200 µl DMSO for intraperitoneal injection or in 1ml 30% SBECD solution (dissolved in GibcoTM Dulbecco's Phosphate Buffered Saline (D-PBS)) for oral administration.

Non-invasive measurement of cardiovascular and respiratory functions

Cardiovascular and respiratory functions were measured using a non-invasive pulse oximeter (MouseOx Plus, Starr Life Sciences Corp., PA, USA). Blood flow parameters shown on figures corresponds to the measured pulse distention, which is the measure of change in blood vessel

volumes in the light path of the sensor, which reflects local blood pressure changes. Rats were anesthetized and the neck region was trimmed using a small animal trimmer to facilitate accurate measurements by size specific collar sensor.

Concentration measurement from tissue samples

Animals were treated *i.p.* or *per os* with MPH-220, over-anesthetized and tissue samples were collected and frozen at -80°C. Tissue samples were thawed and homogenized in D-PBS, and chloroform was added to the homogenate. Samples were thoroughly shaken, vortexed and sonicated. After sonication, samples were centrifuged and the chloroform layer was collected. Chloroform extraction was repeated two more times. Chloroform was drying by evaporation in a fume-hood overnight (48 hours). After chloroform drying, water-acetonitrile solution (50%/50%) was added to the samples, which were again vortexed and sonicated again. Samples were centrifuged and supernatants were collected and transferred into ultra-centrifuge vials and ultracentrifuged at 60,000 rpm, 10°C for 60 minutes before HPLC-MS injection. Peak area of compound in HPLC was determined at 400 nm and concentration of compound was determined from the calibration curve. HPLC-MS conditions were the following: Merck Purosphere STAR RP-18 endcapped 250 mm X 4.6 mm column, mobile phase: isocratic 50% H₂O (0.1% TFA) – 50% ACN (0.09% TFA), injection volume: 20 µl HPLC, flow rate: 0.5 ml/min, run time: 25 min, detection at 260, 280, 300, 400 and 450 nm, capillary voltage: 3.5 kV, cone voltage: 30 V.

Spasticity animal model

Targeted brain damage was performed to establish a rat model of spastic cerebral palsy. Briefly, animals were pre-anesthetized with 4% isoflurane, which was reduced to 2% after the fixation of the animal on the stereotactic apparatus. First, a 2 cm-long longitudinally incision between ears was carried out, which was followed by the cleaning of the surface of the skull by hydrogen peroxide to visualize the Bregma point. Injection coordinates were determined based on *The Rat Brain in Stereotaxic Coordinates*, 6th Edition (Paxinos and Watson, 2007): ML -0.8 mm, AP -10 mm and DV 9.7 mm from the dura. A 25 µl Neuros Syringe (Hamilton, NV, USA) with needle size 22G was used to gently inject 15 µl ethanol for left pyramidal tract lesion. After the injection the syringe was left in place for 10 minutes, followed by its removal from the brain and the sealing of the wound.

Neural network based deep-learning analysis of movements in open-field tests

The over-ground locomotion of the animals was recorded in an 80 by 80 cm wide plastic open-field box using an 8 mm thick transparent Plexiglas as the bottom panel over the course of 15 minutes. The arena was placed on a custom-made wooden frame in order to raise it 1 meter above the ground level, while keeping the transparent bottom unobstructed. A Microsoft Kinect

V2 for XBOX ONE (2013) RGB-D sensor was secured approx. 80 cm below the Plexiglas facing upwards to capture depth information from inside the open-field arena (**Fig. 4B**). The Kinect sensor was connected to a Windows PC (i5-9500F, GeForce GTX 1050 2 GB, 16GB DDR4) placed in a separate room via the official adapter (Kinect Adapter for Windows PC) and a USB extension cable. The Kinect for Windows SDK V2.0.1410.19000 API-s were used to control the Kinect sensor in MATLAB v. R2019b with the Image Acquisition Toolbox Support Package for Kinect for Windows Sensor add-on.

An in-house MATLAB program was used to calibrate the spatial position of the device by measuring the relative distance of the four corners of the arena to the sensor to ensure uniform depth information values in the whole arena during experiments. Another in-house MATLAB program was used for image acquisition by the infrared depth camera (512 x 424 / 30 FPS) and the RGB camera (1920 x 1080 / 30 FPS) simultaneously. Video recordings from the depth camera were stored in .mj2 archives using lossless 16-Bit Motion JPEG 2000 compression, while the RGB camera recordings were stored in MP4 formats to allow easy viewer access. The depth video recordings were subjected to a preprocessing MATLAB script to correct the erroneous depth estimates arising from the time-of-flight depth sensing, such as flying pixels and multipath interference. The modified archives were scaled to preserve intensity values of the region of interest (rat in the arena) and exported as 8-Bit uncompressed AVI videos for further use.

A Resnet-50 deep convolutional neural network was trained to predict distinct body parts (nose, neck, center, right forelimb, left forelimb, right hindlimb, left hindlimb, base of the tail) of the animals on the 8-Bit depth recordings using the DeepLabCut toolbox (Mathis et al., 2018) in the Google Colaboratory python environment. The network training parameters were identical as described in (Nath et al., 2019) using ~1000 frames total for the final training and validation sets (500.000 iteration of training achieved 1.75 mean pixel error for the training and 7.33 mean pixel error for the validation set). A custom MATLAB script was then used to process the previously modified depth archives (25.000 frames / recording) in conjunction with the error corrected numerical output (X and Y coordinates) of the deep learning algorithm of each labeled body part. The animals were first segmented based on the pixel intensity deviation relative to the background. Each frame was then translated and rotated based on the position and angle of the axis between the center of mass of the animal and the position of its nose to create egocentric recording. This transformation and rotation was then carried out on the body part labels as well. The 3 dimensional position of each limb was calculated by combining the transformed output coordinates of the deep neural net with the depth information of the labeled body parts on each frame of the preprocessed and transformed depth recordings. The three dimensional movement maps were exported to further analyses.

In the final algorithm 95% CI least-squares elliptical fittings were computed on the 3D movement maps of each individual limb of the animals and the gait parameters were calculated (**Table S3**). Centroid displacement thresholds on moving average function of 100 frames were used to calculate distinct locomotion regimes (1st Regime: <0.6 pixel deviation, 2nd Regime: >0.6

and <1.2 pixel deviation, 3rd Regime: >1.2 pixel deviation.). The gait parameters were scaled using the Z-score method and subjected to principal component analysis and the results were represented in the 3D PC space together with the 95% CI ellipsoids.

Cylinder assay

Motor functions of spastic rats were tested in an open-top, 21 cm diameter, clear plastic cylinder. Forelimb activity was calculated from number of touches of each forelimb against the wall of the arena. Forelimb touch was defined when the whole palm touched the sidewall of the cylinder. Number of sidewall touches was counted for 3 minutes.

Safety panel measurements

G-protein coupled receptor inhibition and activation was tested in the gpcrMAX panel of DiscoverX[®] Profiling service (Eurofins). Caco-2 assays were carried out by Absorption and Permeability Services at Eurofins Discovery. Predictor[™] hERG Fluorescence Polarization Assay, SelectScreen Kinase Profiling and SelectScreen Nuclear Receptor Profiling was carried out by Thermo Fisher Scientific. Ames MPF[™] (Xenometrix, Switzerland) reverse mutagenicity assay was performed according to the manufacturer's guide on TA98 and TA100 bacterial strains in the absence and presence of phenobarbital/ β -naphthoflavone-induced rat liver S9 fraction. Cytotoxicity measurements were performed with CyQUANT[™] LDH Cytotoxicity assay (Thermo Fisher) according to the manufacturer's protocols with human adult dermal (Gibco, Thermo Fisher) and lung (Cell Applications Inc., CA, USA) fibroblast strains.

Supplementary Text

The broadest available human G-protein-coupled-receptor (GPCR) and kinase panels were used to test MPH-220 inhibition on 168 GPCRs and 484 wild-type and most frequent mutant kinases (**Fig. S13A-B**). Inhibition and activation levels did not approach the threshold used by regulatory agencies confirming the highly selective nature of MPH-220, which supports the safe use of MPH-220 in systemic treatments. We further tested the activation and inhibition of the most important hormone nuclear receptors and MPH-220 proved safe in this regard, too, because hormone receptors were neither activated (**Fig. S13C**) nor inhibited (**Fig. S13D**) due to the lack of receptor binding by MPH-220 (**Fig. S13E**). Cytotoxicity of MPH-220 was also tested on two human adult fibroblast cell lines for two and five days and both 20 μ M and 50 μ M MPH-220 proved non-cytotoxic in both strains (**Fig. S13F**). We also investigated the mutagenicity of MPH-220 by OECD/FDA approved Ames reverse mutagenicity assay up to the solubility limit of MPH-220. We used the two FDA-required bacterial strains sensitive for frameshift and base-pair substitution mutations and neither strain showed any sign of mutagenicity of MPH-220 or

any other derivatives containing a morpholine group (**Fig. S14**). These properties confirmed that MPH-220 is pharmacologically safe, which permits its development toward human clinical trials.

gene	MYH1	MYH2	MYH3	MYH4	MYH6	MYH7	MYH8	MYH9	MYH10	MYH11	MYH13	MYH14
myosin-2 isoform	MyHC IIx/d	MyHC IIa	embryonic skeletal	MyHC IIb	α -cardiac	β -cardiac/MyHC I	perinatal skeletal	NM2A	NM2B	smooth	extraocular	NM2C
human	L	L	L	L	F	F	L	F	F	F	L	F
rat			L	L	F	F		F	F	F		
pig	L	L		L		F						
dog	L	L		L		F	L	F			L	
chicken	L		L					F		F		
rabbit				L						F		
cow	L	L				F			F			
mouse	L		L	L	F	F	L	F	F	F		F

gene	MYSA/MYO2	MYSN
myosin-2 isoform	muscle	non-muscle
Drosophila	F	F
C.elegans	F	

MYH1 (MyHC IIx/d - fast)

human LDIAGFEIFDFNS**L**EQLCINFTNEKL
pig LDIAGFEIFDFNS**L**EQLCINFTNEKL
dog LDIAGFEIFDFNS**L**EQLCINFTNEKL
chicken LDIAGFEIFDFNS**L**EQLCINFTNEKL
cow LDIAGFEIFDFNS**L**EQLCINFTNEKL
mouse LDIAGFEIFDFNS**L**EQLCINFTNEKL
*****:*****

MYH2 (MyHC IIa - fast)

human LDIAGFEIFDFNS**L**EQLCINFTNEKL
pig LDIAGFEIFDFNS**L**EQLCINFTNEKL
dog LDIAGFEIFDFNS**L**EQLCINFTNEKL
cow LDIAGFEIFDFNS**L**EQLCINFTNEKL
*****:*****

MYH3 (embryonic skeletal - fast)

human LDIAGFEIFEYNS**L**EQLCINFTNEKL
rat LDIAGFEIFEYNS**L**EQLCINFTNEKL
mouse LDIAGFEIFEYNS**L**EQLCINFTNEKL
chicken LDIAGFEIFEYNS**L**EQLCINFTNEKL
*****:*****

MYH4 (MyHC IIb - fast)

human LDIAGFEIFDFNS**L**EQLCINFTNEKL
pig LDIAGFEIFDFNS**L**EQLCINFTNEKL
dog LDIAGFEIFDFNS**L**EQLCINFTNEKL
rabbit LDIAGFEIFDFNS**L**EQLCINFTNEKL
rat LDIAGFEIFDFNT**L**EQLCINFTNEKL
mouse LDIAGFEIFDFNT**L**EQLCINFTNEKL
*****:*****

MYH6 (α -cardiac)

human LDIAGFEIFDFNS**F**EQLCINFTNEKL
rat LDIAGFEIFDFNS**F**EQLCINFTNEKL
mouse LDIAGFEIFDFNS**F**EQLCINFTNEKL
*****:*****

MYH7 (β -cardiac, MyHC I – slow)

human LDIAGFEIFDFNS**F**EQLCINFTNEKL
rat LDIAGFEIFDFNS**F**EQLCINFTNEKL
pig LDIAGFEIFDFNS**F**EQLCINFTNEKL
dog LDIAGFEIFDFNS**F**EQLCINFTNEKL
cow LDIAGFEIFDFNS**F**EQLCINFTNEKL
mouse LDIAGFEIFDFNS**F**EQLCINFTNEKL
*****:*****

MYH8 (perinatal skeletal)

human LDIAGFEIFDFNS**L**EQLCINFTNEKL
dog LDIAGFEIFDFNS**L**EQLCINFTNEKL
mouse LDIAGFEIFDFNS**L**EQLCINFTNEKL
*****:*****

MYH9 (NM2A)

human LDIAGFEIFDLNS**F**EQLCINFTNEKL
rat LDIAGFEIFDLNS**F**EQLCINFTNEKL
dog LDIAGFEIFDLNS**F**EQLCINFTNEKL
mouse LDIAGFEIFDLNS**F**EQLCINFTNEKL
chicken LDIAGFEIFEYNS**F**EQLCINFTNEKL
*****:*****

MYH10 (NM2B)

human LDIAGFEIFEYNS**F**EQLCINFTNEKL
rat LDIAGFEIFEYNS**F**EQLCINFTNEKL
cow LDIAGFEIFEYNS**F**EQLCINFTNEKL
mouse LDIAGFEIFEYNS**F**EQLCINFTNEKL
*****:*****

MYH11 (smooth)

human LDIAGFEIFEVNS**F**EQLCINFTNEKL
rat LDIAGFEIFEVNS**F**EQLCINFTNEKL
rabbit LDIAGFEIFEVNS**F**EQLCINFTNEKL
mouse LDIAGFEIFEVNS**F**EQLCINFTNEKL
chicken LDIAGFEIFEINS**F**EQLCINFTNEKL
*****:*****

MYH13 (extraocular skeletal)

human LDIAGFEIFDFNS**L**EQLCINFTNEKL
dog LDIAGFEIFDFNS**L**EQLCINFTNEKL
*****:*****

MYH14 (NM2C)

human LDIAGFEIFQLNS**F**EQLCINFTNEKL
mouse LDIAGFEIFQLNS**F**EQLCINFTNEKL
*****:*****

MYSA/MYO2 (muscle)

Drosophila LDIAGFEIFEYNG**F**EQLCINFTNEKL
C.elegans LDIAGFEIFDFNS**F**EQLCINFTNEKL
*****:*.**** **.*

MYSN (non-muscle)

Drosophila LDMAGFEIFEYNS**F**EQLCINFTNEKL

Fig. S1. Sequence analysis of myosin-2 isoforms from different species. Related to Figure 1

The tables show the amino acid residue at the starting point of the HP-helix in myosin-2 isoforms expressed from different MYH genes in eight vertebrate species and the muscle and non-muscle myosin-2 isoforms in *D. melanogaster* and *C. elegans* invertebrate species. The alignments below the tables represent the sequence environment of the relevant Leu (blue L) or Phe (black F) residue, including the switch-2 loop (red) and the N-terminal part of the HP-helix (light orange). These data clearly show that all fast skeletal myosin-2 isoforms in all species contain Leu in the morpholine-interacting position, while Phe is present in all slow type myosin-2s including both cardiac isoforms at this position. The characteristic difference is even more pronounced when comparing the neighboring residues in the HP-helix, which are practically invariant in all myosin isoforms and species.

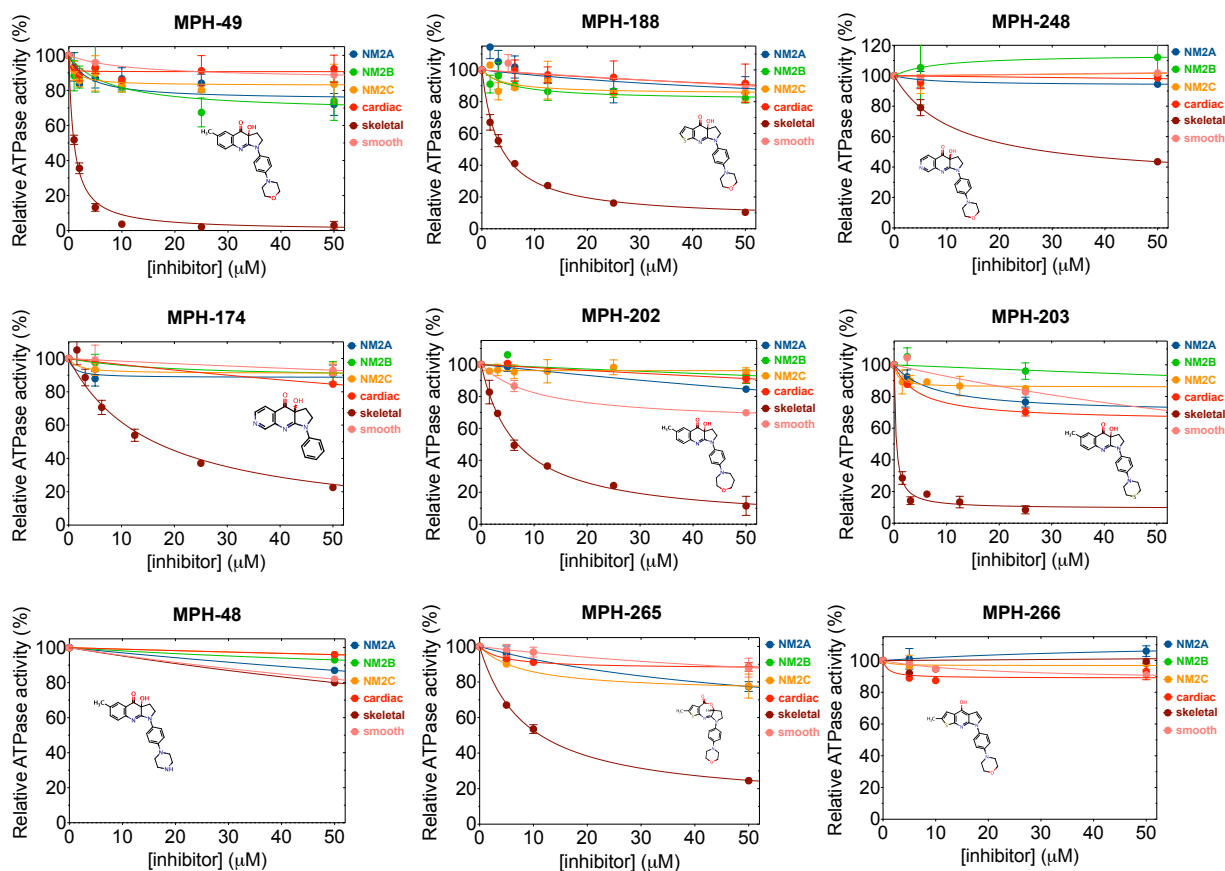


Fig. S2. Inhibitory properties of different MPH-220 derivatives. Related to Figure 1.

Relative ATPase activities are shown for different MPH-220 derivatives tested during the development of MPH-220. MPH-49 is the morpholine derivative of blebbistatin, which shows selective inhibition; however, its solubility remained blebbistatin-like (less than 50 μM in aqueous solutions). MPH-188 and MPH-248 are morpholine derivatives on different scaffolds of the patented MPH-family. MPH-188 showed drastic improvement in solubility (1 mM in aqueous solutions), but its IC_{50} value for skeletal myosin was slightly worse than that of MPH-220. MPH-248 retained skeletal myosin specificity of the pyridine ring containing core (MPH-174), but its total inhibition and IC_{50} values remained worse than those of MPH-220. We also tried to modify the structure of the morpholine ring by using homomorpholine (MPH-202), thiomorpholine (MPH-203) or piperazine (MPH-48) substituents, but neither molecule showed better properties than the morpholine counterpart (MPH-49). The IC_{50} of MPH-203 was promising; however, its solubility was even lower than that of MPH-49, suggesting that the optimal ring structure for selective and efficient inhibition is the morpholine ring. We also tried to modify the ring structure of the tricyclic core, but neither modification showed improved properties, confirming that MPH-220 is the optimal structure.

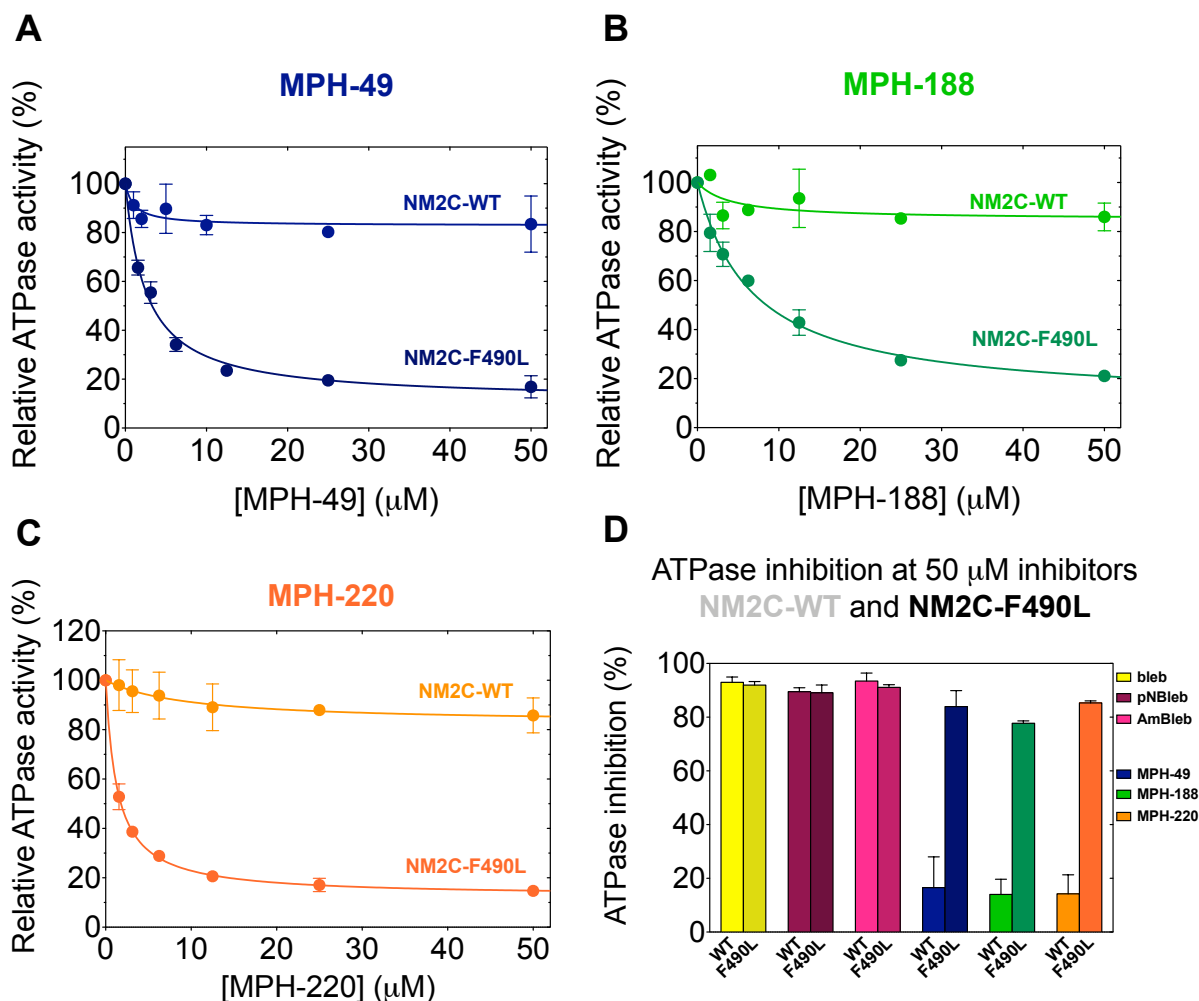


Fig. S3. Contrary to wild-type NM2C, the NM2C variant harbouring the F490L substitution is sensitive to inhibition with morpholine group containing MPH-220 derivatives. Related to Figure 1.

ATPase activity was measured with MPH-49 (A), MPH-188 (B) and MPH-220 (C, same dataset as in Fig. 1I) on wild type and F490L variant form of NM2C. All three derivatives showed insignificant inhibition on the wild type form, while all three inhibited the F490L form efficiently. Importantly, when non-selective blebbistatin derivatives with small modifications on the D-ring (blebbistatin – yellow, para-nitroblebbistatin – purple, para-aminoblebbistatin – pink) were used, both wild type and F490L NM2C forms were inhibited identically (D). These data confirm that the selectivity observed for MPH-220 is due to the specific combination of morpholine substitution on the inhibitor and the unique Leu in the HP-helix of fast skeletal muscle myosin isoforms (cf. Fig. 1B, Fig. S1).

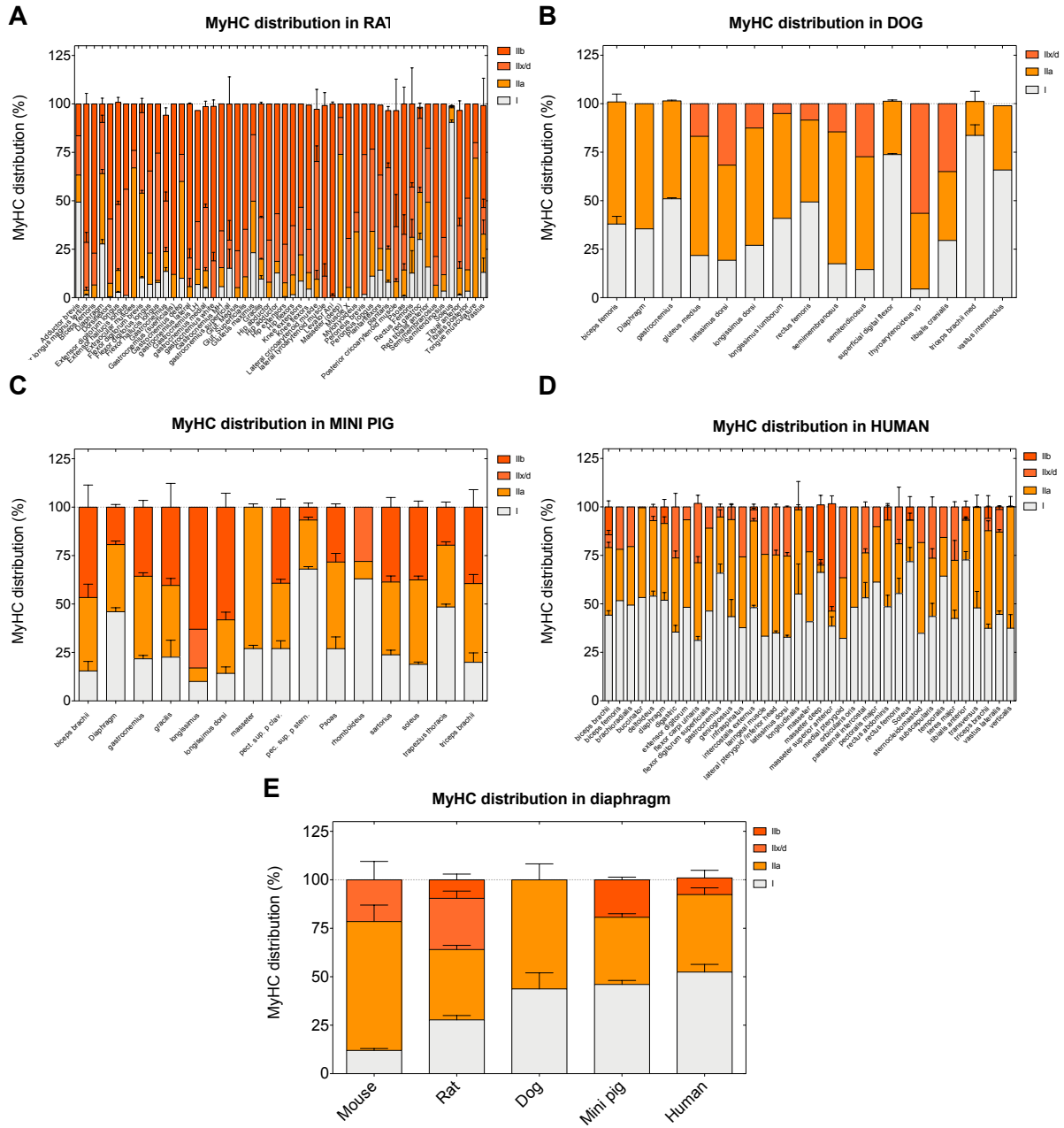


Fig. S4. Myosin-2 isoform distribution within different muscle types in different species. Related to Figure 1.

Literature-based analysis of myosin-2 isoform composition – determined by SDS-PAGE or immune/enzyme histochemistry – of different muscles in rat (A), dog (B), mini pig (C) and human (D) show significant differences in the proportion of the slow isoform (MyHC I, gray) between the species. While rat muscles contain predominantly fast isoforms (MyHC IIa, IIb, IIx/d, orange), the ratio of fast isoforms in human muscles is between 40-70%. Distributions in dogs and mini-pigs are in between the rat and human levels. These differences bear important

consequences on the expected effect size in different species and may require unique consideration of dosage in non-clinical studies on different species (e.g. rats vs. dogs/pigs). The relatively high proportion of slow isoform in human muscles also has important positive consequence on the effect profile of an MPH-220 based anti-spastic drug, because overdosing-related complete muscle tone loss is not expected to occur due to the residual non-inhibited slow myosin contractions. This latter condition confers a huge advantage over the currently used nervous system targeting muscle relaxants, where temporary but complete immobility can readily in case of slight overdose. The large difference in slow isoform proportion can also be seen in the diaphragm of different species (**E**), which indicates that MPH-220 will be even safer for respiratory functions in humans than in rats.

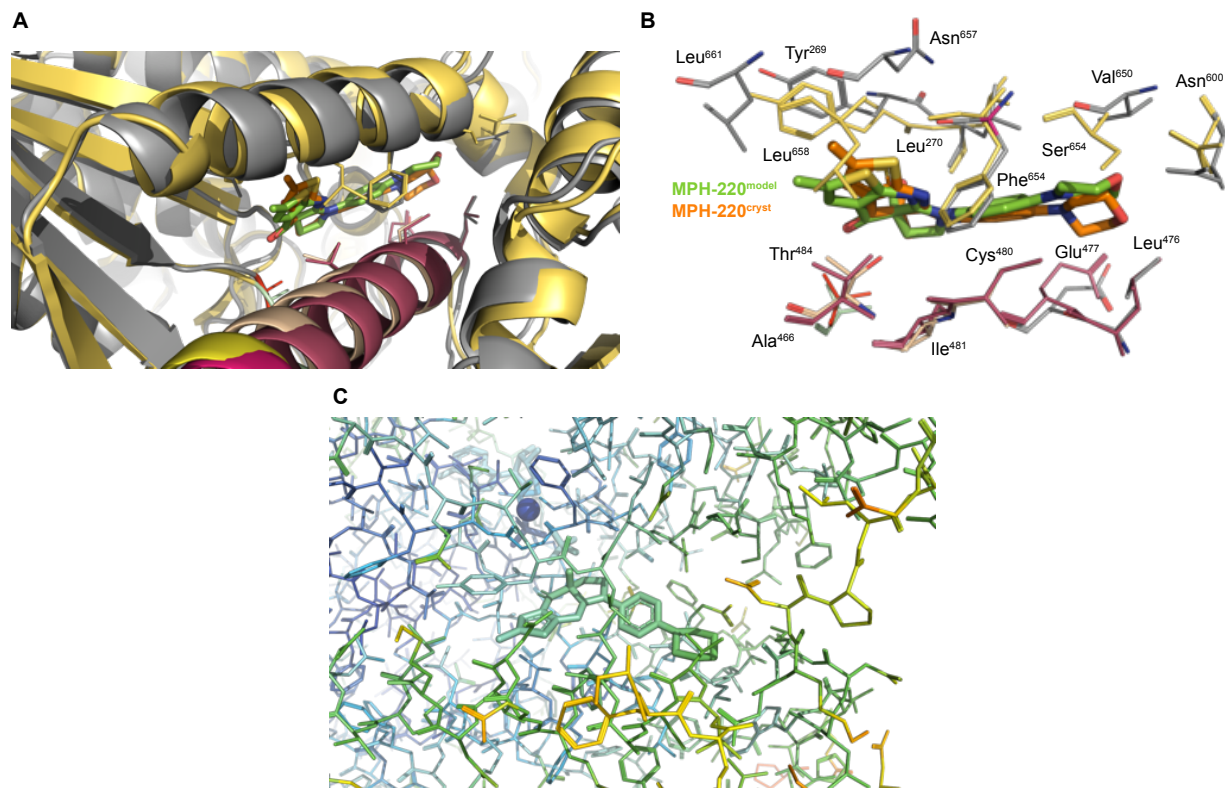


Fig. S5. Crystal structure of MyHC IIb is similar to the modeled structure used for inhibitor development. Related to Figure 2.

(A) Cartoon representation of the crystal structure of MyHC IIb (gray/beige), and the superimposed modelled structure of MyHC IIa from molecular dynamic simulations (yellow/maroon). MPH-220 binding site reveals that the position and orientation of MPH-220 in the crystal structure (orange) and in the modeled structure (green) is similar. Amino acid residue carbons in gray (crystal structure) and maroon (model), and carbons for MPH-220 in orange (crystal structure) and green (model) are shown. (B) Close-up of the MPH-220 binding site reveals that HP-helix position is well predicted; in particular, Leu⁴⁷⁶ position is very similar. The alignment also reveals a moderate shift in MPH-220 position between the homology model and the crystal structure; in particular we see slightly different position and orientation of the morpholino group. Still, the homology model predicts well the sub-pocket explored by this cycle; residues Leu⁴⁷⁶, Glu⁴⁷⁷, Cys⁴⁸⁰, Asn⁶⁰⁰ and Val⁶⁵⁰ interact indeed with the morpholino group in both crystal structure and homology model. These results confirm that the modelled structure that we used for inhibitor development (cf. **Fig. 1**, **Fig. S2**) is reliable and the results from those experiments are trustworthy. (C) Close-up view of the crystal structure with bound MPH-220 colored according to B-factors from 21.1 Å² (dark blue) to 125.2 Å² (red). ADP, VO₄ and MPH-220 are represented by thicker lines, the sphere represents the Mg²⁺ ion.

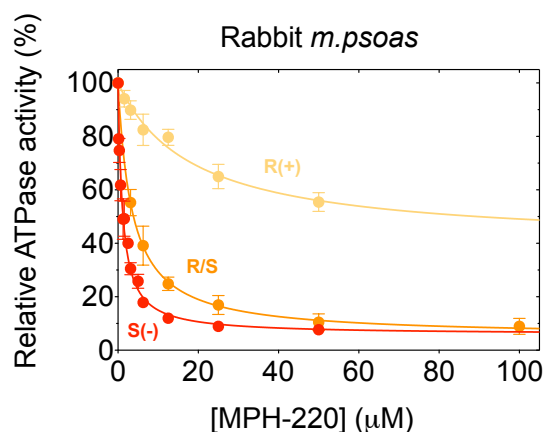


Fig. S6. ATPase inhibition of myosin preparation from rabbit *m.psoas* by the S(-), R(+) enantiomers and the racemic mixture of MPH-220. Related to Figure 3.

(A) Skeletal muscle myosin from rabbit *m.psoas* (containing 95% fast MyHC isoforms) is efficiently inhibited by S(-) (red, $IC_{50,S(-)} = 1.1 \pm 0.1 \mu\text{M}$, $I_{\text{total},S(-)} = 94 \pm 1\%$) and the racemic mixture of MPH-220 (orange, $IC_{50,R/S} = 3.4 \pm 0.2 \mu\text{M}$, $I_{\text{total},R/S} = 95 \pm 1\%$). The R(+) enantiomer is not effective, because its IC_{50} value is an order of magnitude higher than that of the S(-) enantiomer, and the total inhibition could not be achieved (yellow, $IC_{50,R(+)} = 19 \pm 3 \mu\text{M}$, $I_{\text{total},R(+)} = 60 \pm 4\%$). Data are mean \pm SD; $n=3-6$.

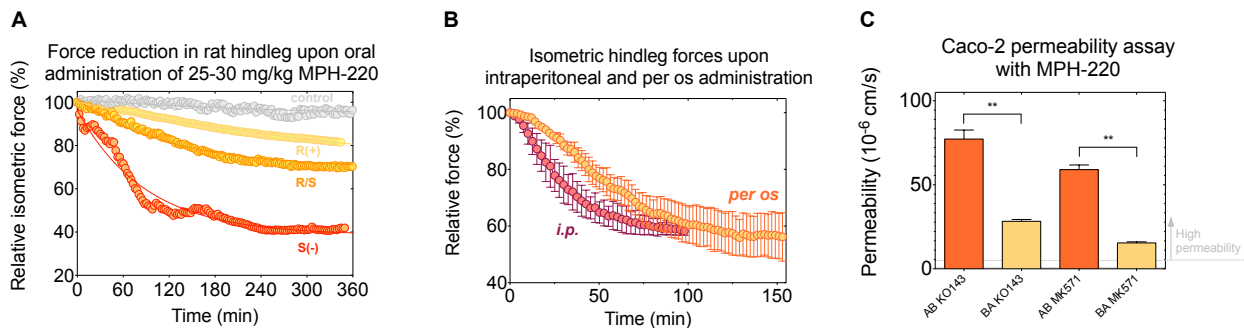


Fig. S7. Isometric force reduction by MPH-220 after intraperitoneal and oral administration. Related to Figure 3.

(A) Isometric force reduction in rat hindleg after oral MPH-220 treatment: $\Delta F_{S(-)} = 58\%$, $\Delta F_{R(+)} = 36\%$, $\Delta F_{R/S} = 32\%$, $\tau_{S(-)} = 88$ min, $\tau_{R(+)} = 121$ min, $\tau_{R/S} = 461$ min; muscle fatigue in the control animals: $\Delta F_{\text{contr}} = 8\%$, $\tau_{\text{contr}} = 323$ min. (B) 18 mg/kg MPH-220 was administered to anesthetized rats by intraperitoneal injection in 200 μl DMSO (pink circles) or orally through a gavage tube in 30% SBEDC (orange circles). Isometric force decrease rates were very similar ($\tau_{i.p.} = 34$ min) except that oral administration resulted in a 17-minute leg phase – corresponding to absorption of MPH-220 – followed by force decrease phase ($\tau_{p.o.} = 53$ min). These observations support high gastrointestinal permeability of MPH-220, which was further confirmed by *in vitro* Caco-2 permeability assay (cf. Fig. 3E). (C) Caco-2 permeability assay in the apical-to-basolateral (AB, orange) and basolateral-to-apical (BA, light orange) direction in the presence of two different transporter inhibitors.

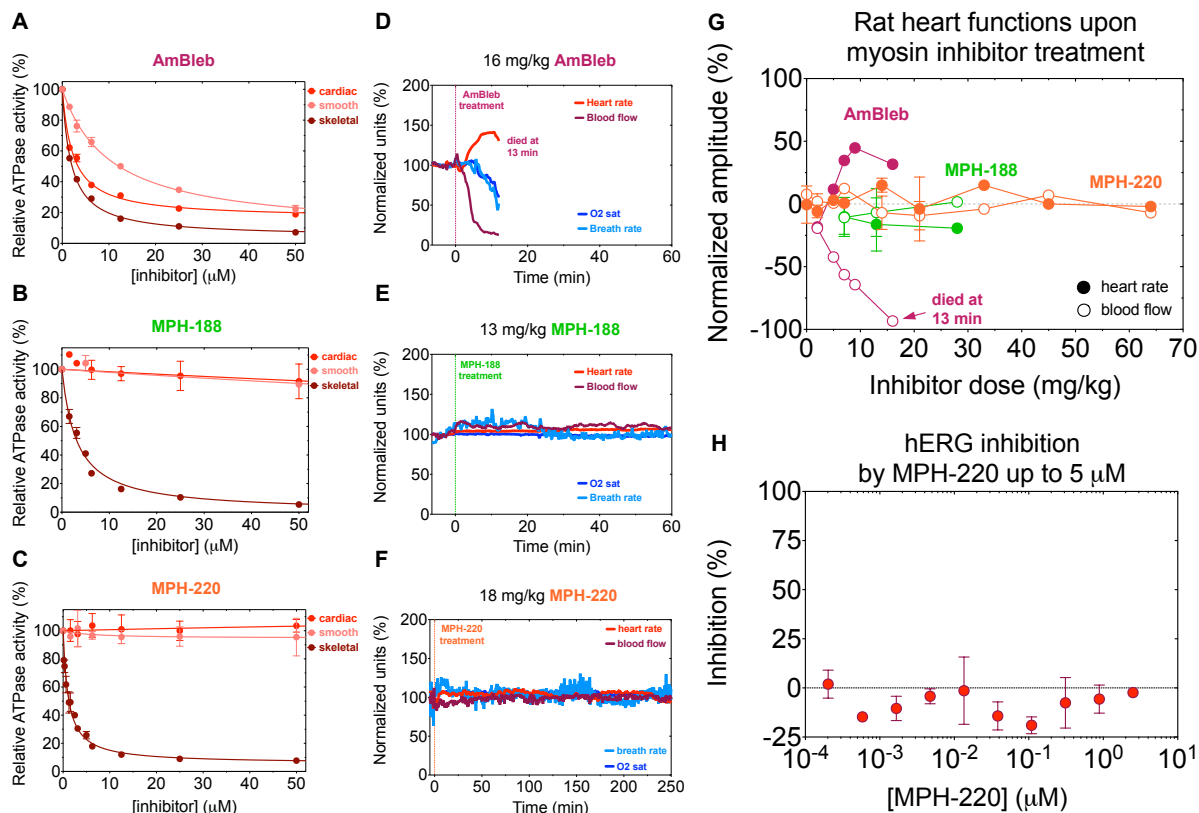


Fig. S8. Unlike the non-selective myosin-2 inhibitor, AmBleb, morpholine derivatives do not perturb cardiovascular and respiratory functions in the effective dose range. Related to Figure 3.

(A-C) ATPase activity of skeletal (brown), cardiac (red) and smooth (pink) muscle myosins, measured in the presence of non-selective para-aminoblebbistatin (AmBleb, A), MPH-188 (B) and MPH-220 (C). (D-F) All three inhibitors were administered to rats in different concentration ranges and cardiovascular (heart rate, blood flow) and respiratory functions (breath rate, oxygen saturation) were monitored. 16 mg/kg AmBleb killed the animals within 15 minutes due to heart failure (D), while neither 13 mg/kg MPH-188 (E) nor 18 mg/kg MPH-220 (F) had any significant effect on cardiovascular and respiratory functions. Note that we measured MPH-220 effect on longer time scales (parallel with force measurements). (G) We repeated the experiments several times and found that MPH-220 does not affect cardiac functions to a greater extent than the solvent excipient during the long anesthetic period (cf. Fig. 2F-G). Data are mean \pm SD, $n=1-4$. (H) hERG potassium channel inhibition measurement up to 5 μM MPH-220. We measured hERG inhibition up to 5 μM , because the concentrations of MPH-220 in cardiac tissue even upon treatment with high doses (up to 130 mg/kg) were in this concentration range (3-7 μM). At this concentration range we did not observe inhibition of hERG potassium channels and we did not observe any concentration dependence of inhibition on cardiomyocytes, which would otherwise potentiate a drug candidate for QT prolongation leading to life-threatening arrhythmias (Pollard et al., 2010).

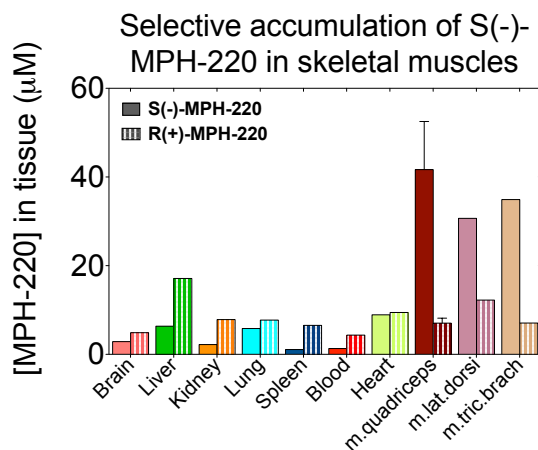


Fig. S9. S(-)-MPH-220 accumulates in muscle tissues with higher tendency than the R(+) enantiomer. Related to Figure 3.

Six hours after oral treatment with 25 mg/kg S(-) and R(+) enantiomers of MPH-220, rat tissue samples were analyzed and remarkable difference in accumulation could be observed. 3-6-times more S(-) enantiomer was accumulated in skeletal muscle tissues than R(+) enantiomer. However, this difference was not due to incomplete absorption of the R(+) enantiomer as the concentration of both enantiomers was approximately the same in all other tissues. Moreover, R(+)-MPH-220 concentration was even higher in liver, spleen and blood.

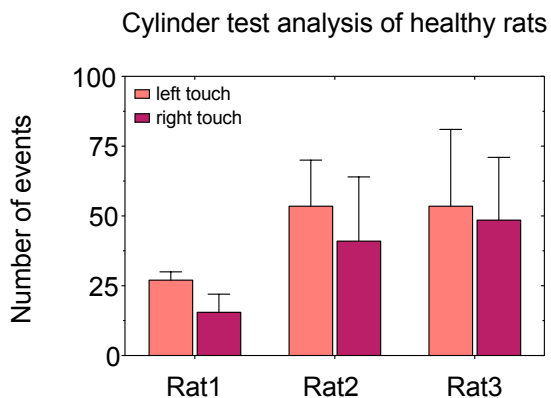


Fig. S10. Cylinder test analysis of healthy rats show large individual variance in the tendency to stand up. Related to Figure 4.

Cylinder assay was carried out on three healthy littermates of the pyramidal tract damaged rats. Individual differences could be observed both in their intention to stand up and in general activities. All three rats were tested two times with 6 hours difference between the two measurements. Importantly, the number of prancing was in the range in which the spastic rats showed improvement after MPH-220 treatment (cf. **Fig 4D**), suggesting that MPH-220-reduced spasticity in the hindlegs enabled the rats to use their legs normally in the cylinder assay.

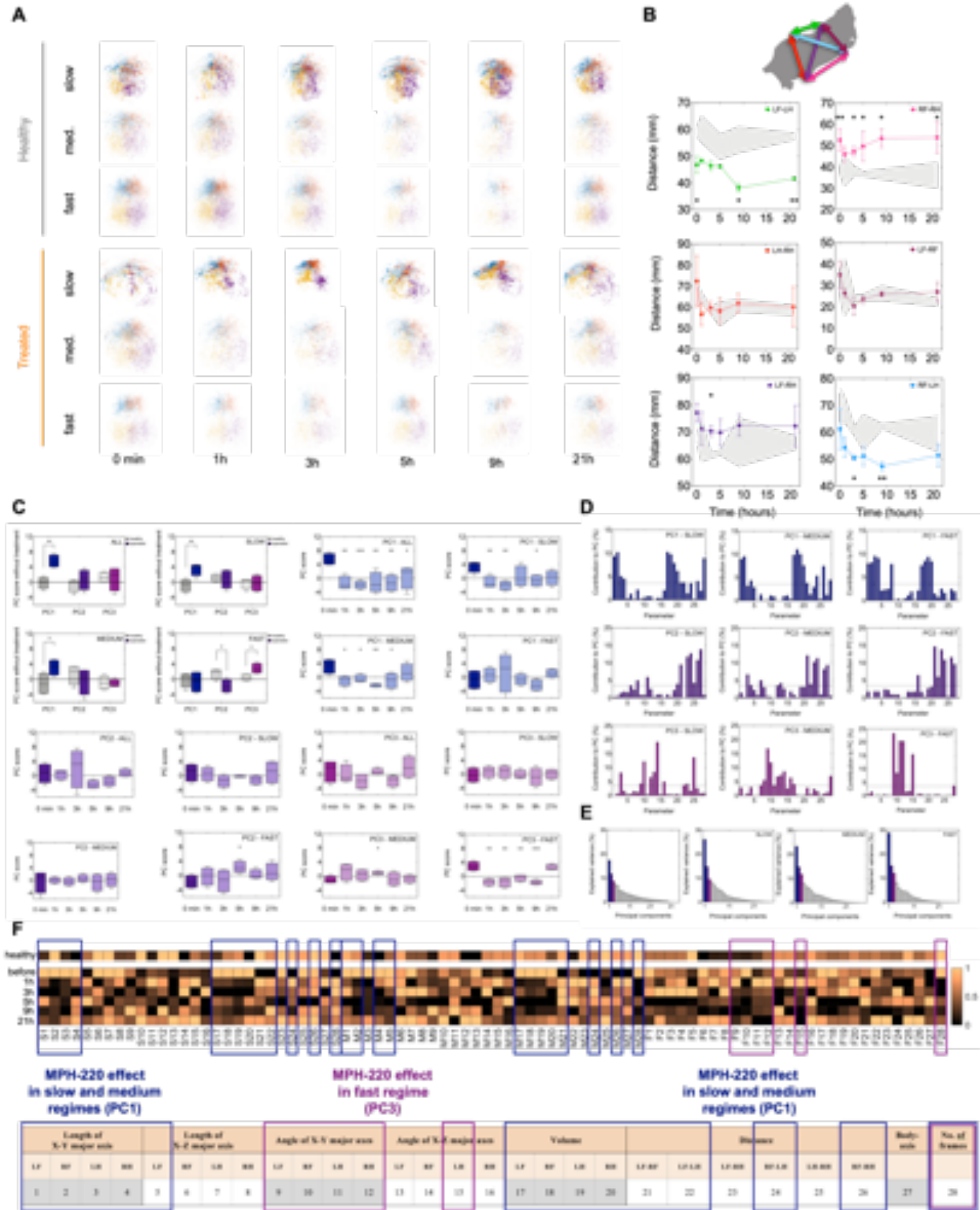


Fig. S11. Gait analysis of MPH-220 treated rats. Related to Figure 4 and Figure 5

(A) Paw position distribution of healthy (upper three rows) and treated (lower three rows) animals in the three speed-regimes (cf. **Table S3**), 1, 3, 5, 9 and 21 hours after the first

measurement (healthy control) or before and 1, 3, 5, 9 and 21 hours after 20 mg/kg oral MPH-220 treatment. **(B)** Averaged distances between the paws in each frame of the 3D recordings in healthy (gray band) and treated (colored dots) animals; green: left fore- and hindlimbs, pink: right fore- and hindlimbs, red: left and right hindlimbs, maroon: left and right forelimbs, purple: left fore- and right hindlimbs, blue: right fore- and left hindlimbs. Schematic representation of distances is shown above the plots. Statistical analysis show that left fore- and hindlimbs are significantly closer in the operated rats than in the healthy animals, however, 1-5 hours after MPH-220 treatment the difference becomes insignificant. The right fore- and hindlimbs are significantly farther in the operated rats before treatment, which becomes non-significant 1 hour after MPH-220 treatment. These together indicate that MPH-220 treatment resulted in a significantly straightened body axis. Data are mean \pm SD; n=2. **(C)** Principal component (PC) analysis: PC1, PC2 and PC3 scores of healthy (gray) and operated (colored bars) rats in all, slow, medium-speed and fast movement regimes (upper left quartet). PC1 (blue, upper right quartet), PC2 (eggplant, lower left quartet) and PC3 (purple, lower right quartet) scores before (darker) and after (lighter) 20 mg/kg oral MPH-220 treatment in all, slow, medium-speed and fast movement regimes. Box plots with min-to-max whiskers, n=4. **(D)** Parameter contributions to PC1 (upper row), PC2 (middle row) and PC3 (lower row) in the slow (left column), medium-speed (middle column) and fast (right column) movement regimes. Dotted lines represent the threshold for major contributions to PC (3.57%). Box plots with min-to-max whiskers, n=4. **(E)** Explained variance in all, slow, medium-speed and fast movement regimes; PC1, PC2 and PC3 are colored according to panels C-D. **(F)** The computed gait parameters were scaled (Z-score) and averaged. The columns represent the individual gait parameters (1-28, cf. **Table S3** copied below the heatmap) in the slow (S1-28), medium-speed (M1-28) and fast (F1-28) movement regimes. The separate row represents the average of healthy animals at zero minute, and the other six rows represent the parameter scores before and 1, 3, 5, 9 and 21 hours after MPH-220 treatment (n=4). PC analysis revealed that in the slow regime MPH-220 has the largest effect on X-Y axis length and the consequent volumes of the ellipsoids representing paw positions in 3D and certain distances between the centers of ellipsoids (blue brackets) contributing to PC1; in the fast regime MPH-220 has the largest effect on the angles of the ellipsoids (purple brackets) contributing to PC3.

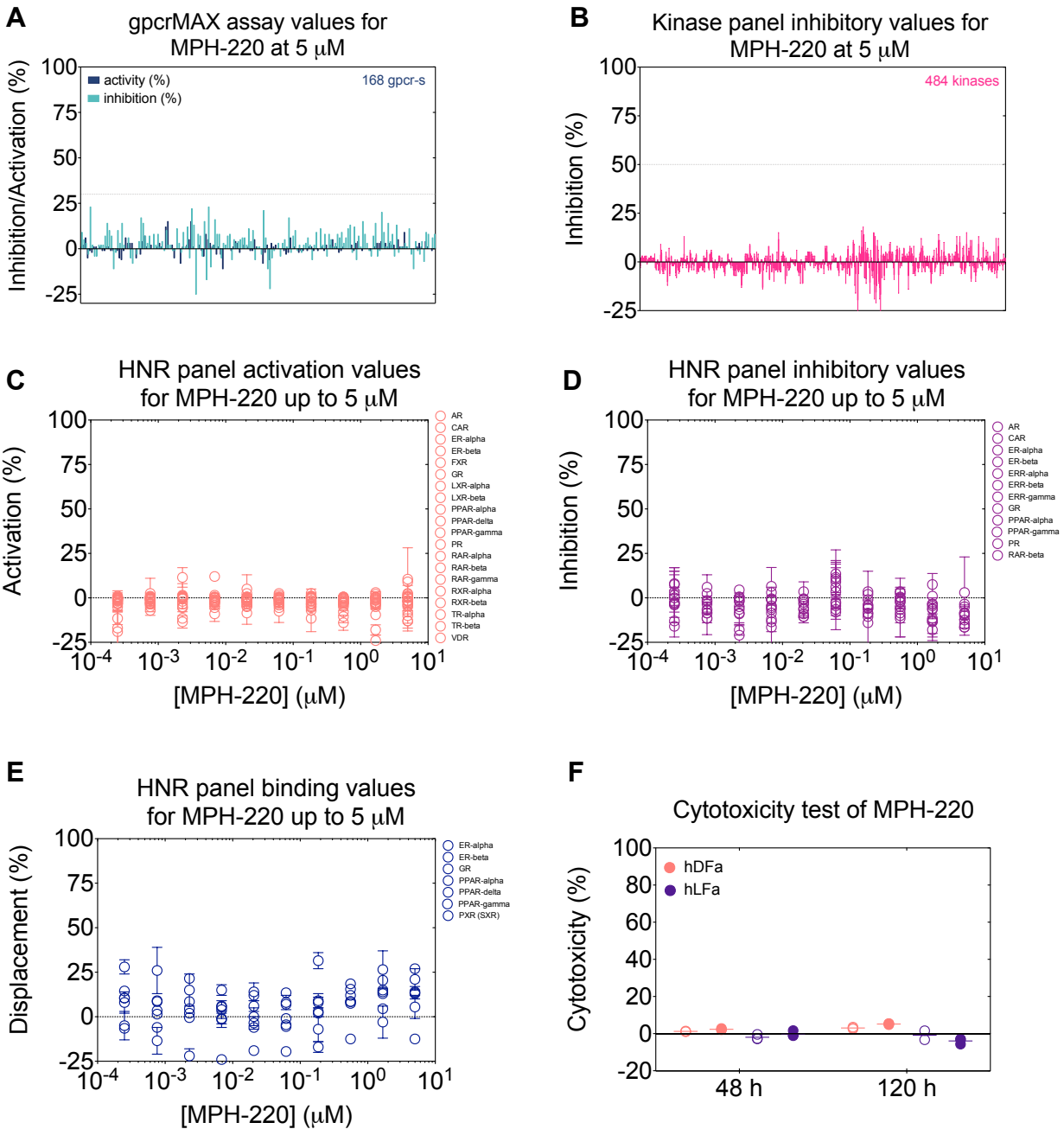


Fig. S12. Safety profiling of MPH-220 supports further drug development due to lack of mutagenicity and interaction with off-target enzymes. Related to STAR Methods.

(A) We tested the effects of 5 μ M MPH-220 on 186 different human G-protein-coupled-receptors (GPCRs) covering 60 different receptor families including adrenergic, dopamine, P2Y and serotonin receptor families (by DiscoverX-Eurofins). According to the highly selective nature of MPH-220, neither GPCR was inhibited or activated above 30%, which is a standard reference threshold for hit compounds. (B) Beside the gpcrMAX panel, inhibition of 484 kinases

was measured in the presence of 5 μM MPH-220. Neither kinase was inhibited by more than 20%, which indicates that MPH-220 does not interfere with signal the signal transduction pathways in human cells. This Select Screen Kinase Profiling panel (by Thermo Fisher) contains all available wild-type and the most abundant mutant forms of human kinases. (C-E) MPH-220 was also tested on 23 human hormone nuclear receptors (HNR) at 5 μM concentration (by Thermo Fisher). In agreement with the kinase and GPCR results, all investigated receptors remained unaffected by MPH-220 due to the lack of significant binding to any of the HNRs. (F) Cytotoxicity was measured with CyQUANTTM LDH Cytotoxicity assay on human adult dermal fibroblast (hDFa, pink) and human adult lung (hLFa, purple) fibroblast cell lines in the presence of 20 μM (open circles) and 50 μM (closed circles) MPH-220 for 48 and 120 hours. MPH-220 was not toxic to either fibroblast strain at any time point or concentration, confirming its safe use in further developments.

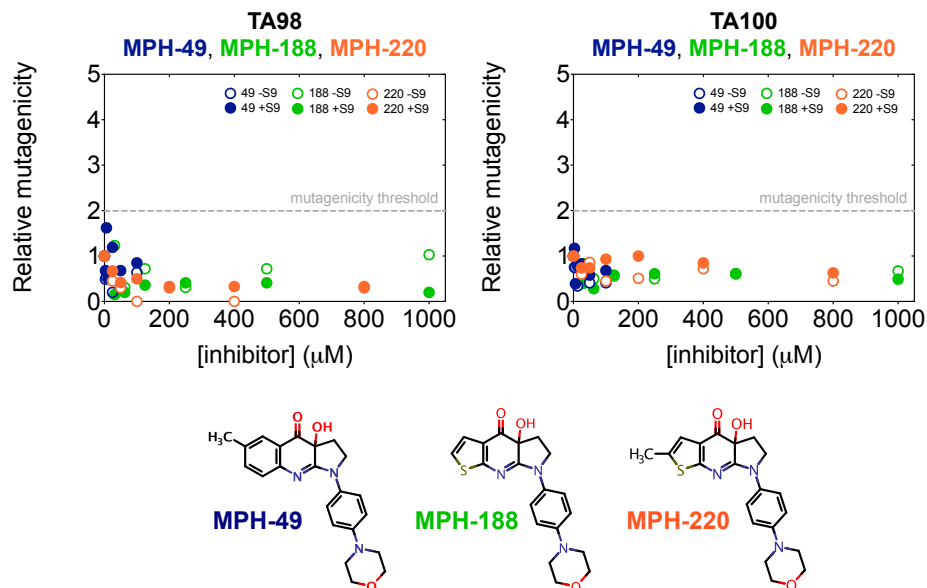


Fig. S13. Morpholine derivatives of MPH-220 do not show mutagenic properties in Ames reverse mutagenicity assays. Related to STAR Methods.

As one of the most important requirements for a lead compound, mutagenicity was measured by the OECD/FDA approved Ames reverse mutagenicity assay using the two most sensitive bacterial strains for testing frameshift (TA98, dark blue) and base-pair substitution (TA100, light blue) mutation both in the absence (open circles) and presence (closed circles) of activated rat liver S9 fraction. Relative mutagenicity did not show MPH-220 concentration dependency and, more importantly, experiments on neither strain resulted in any data points above the threshold (gray dotted line). Besides MPH-220 we also tested the mutagenicity of the other two morpholine derivatives of MPH-220 (cf. **Fig. S2-3**) to elucidate whether the lack of mutagenicity is associated with the morpholine group. Neither MPH-49 nor MPH-188 showed concentration dependent increase in mutagenicity levels and, more importantly, neither showed in data points above the OECD/FDA threshold. Lack of mutagenicity was observed for both TA98 and TA100 *S.typhimurium* strains both in the absence and presence of liver S9 fraction, suggesting that neither the inhibitors nor their major metabolites are mutagenic, which supports safe development of MPH-220 toward human clinical phases.

Myosin-2 isoform	Variant	Source	Species	Length	Modification	ATPase activity* (uninhibited)	IC _{50,MPII-220} **	Maximal inhibition**
NM2A	wt	Sf9-expression	human	S1, M ¹ -R ⁷⁷⁵	AS-linker, α -actinin, FLAG-tag	0.048 \pm 0.008 s ⁻¹ (n=44, 9 preps) ^a	ND ^{***}	ND ^{***}
NM2B	wt, B(0)	Sf9-expression	human	S1, M ¹ -R ⁷⁸²	AS-linker, α -actinin, FLAG-tag	0.021 \pm 0.005 s ⁻¹ (n=49, 11 preps) ^a	1.7 \pm 1.6 μ M	16 \pm 2 %
NM2C	wt, C(0)	Sf9-expression	human	S1, M ¹ -R ⁷⁹⁹	AS-linker, α -actinin, FLAG-tag (Heissler and Manstein, 2011)	0.056 \pm 0.008 s ⁻¹ (n=20, 4 preps) ^a	10 \pm 9 μ M	17 \pm 8 %
NM2C	F490L, C(0)	Sf9-expression	human	S1, M ¹ -R ⁷⁹⁹	AS-linker, α -actinin, FLAG-tag	0.049 \pm 0.002 s ⁻¹ (n=11, 2 preps)	1.3 \pm 0.1 μ M	87 \pm 1 %
β -cardiac myosin	wt	heart, left ventricle	bovine	S1, α -chymotr. dig.		0.43 \pm 0.09 s ⁻¹ (n=12, 2 preps)	ND ^{***}	ND ^{***}
β -cardiac myosin	wt	C ₂ C ₁₂ -expression	human	S1, M ¹ -R ⁸⁰⁸	GSG-linker, eGFP (Kawana et al., 2017)	1.9 \pm 0.2 s ⁻¹ (n=11, 1 prep)	4.8 \pm 3.5 μ M (0.60 \pm 0.02 μ M; blebbistatin)	10 \pm 2 % (98 \pm 1 %; blebbistatin)
β -cardiac myosin	wt	heart, left ventricle	human	S1, α -chymotr. dig.		ND ^c (n=3, 1 prep)	ND ^{***} (0.95 \pm 0.02 μ M; blebbistatin)	ND ^{***} (99.7 \pm 0.4 %; blebbistatin)
Smooth muscle myosin	wt	gizzard	chicken	S1, papain dig.		0.50 \pm 0.03 s ⁻¹ (n=17, 2 preps)	6.2 \pm 12 μ M	5 \pm 3 %
Fast skeletal myosin	wt	<i>m.psoas</i>	rabbit	S1, α -chymotr. dig.		3.7 \pm 0.8 s ⁻¹ (n=20, 3 preps)	1.1 \pm 0.1 μ M	94 \pm 1 %
Mixed (28% fast isoforms) ^b	wt	<i>m.soleus</i>	human	full-length		ND ^c (n=3, 1 prep)	6.7 \pm 1.5 μ M ^d	29 \pm 2 % ^d
Mixed (28% fast isoforms) ^b	wt	<i>m.vastus lateralis</i>	human	full-length		ND ^c (n=18, 6 preps)	1.2 \pm 0.1 μ M (0.84 \pm 0.05 μ M; blebbistatin)	70 \pm 1 % (98 \pm 1 %; blebbistatin)

Table S1. Properties of the applied proteins. Related to Figure 1.

*ATPase activity in the presence of 1% DMSO and 25 μ M F-actin, mean \pm SD is shown

**Inhibitory parameters determined in measurements shown in Fig. 1, mean \pm SD is shown (n= 3-12)

***ND: not-determined reliably due to low levels or lack of inhibition

^aATPase activity of the α -actinin containing human NM2C-S1(C0) construct(Heissler and Manstein, 2011) was 3-10-times lower lower than that of the HMM and full-length variants(Billington et al., 2013; Zhang et al., 2017), which was also reflected in the ATPase activities of our NM2A and NM2B constructs. ATPase activities of S1 variants of NM2A(Kovacs et al., 2003), NM2B(Wang et al., 2003) and NM2C(Heissler and Manstein, 2011) are also 3-6 times higher than the α -actinin containing constructs used here.

^bLiterature-based species dependent MyHC distribution is demonstrated in Fig. S4.

^cND: not-determined due to very low amount of myosin content in the human biopsies – only relative ATPase activity was measured

^dBlebbistatin inhibition was not measured due to limited sample size

Pre-power-stroke (ADP.VO ₄) state	MyHC IIb + MPH-220
Data collection	
Space group	P 2 ₁ 2 ₁ 2 ₁
Cell dimensions	
<i>a</i> , <i>b</i> , <i>c</i> (Å)	49.6 119.4 176.6
α, β, γ (°)	90.0 90.0 90.0
Resolution (Å)	88.3 - 3.3 (3.4 - 3.3)*
<i>R</i> _{merge}	0.003722 (0.2293)
<i>I</i> / σ <i>I</i>	10.46 (2.42)
CC _{1/2}	0.999 (0.939)
Completeness (%)	99.80 (99.88)
Redundancy	2.0 (2.0)
Refinement	
Resolution (Å)	3.3
No. reflections	total: 34625 (3374) unique: 17313 (1687)
<i>R</i> _{work}	0.2260 (0.3450)
<i>R</i> _{free}	0.2464 (0.4555)
Non-hydrogen atoms	7474
Protein	7382
Ligand/ion	60
Water	32
<i>B</i> -factors	100.49
Protein	100.73
Ligand/ion	91.05
Water	62.66
R.m.s. deviations	
Bond lengths (Å)	0.015
Bond angles (°)	1.55

Table S2. Data collection and refinement statistics (molecular replacement). Related to Figure 2.

Data from one crystal. *Values in parentheses are for highest-resolution shell.

Length of X-Y major axis				Length of X-Z major axis				Angle of X-Y major axes				Angle of X-Z major axes				Volume				Distance						Body-axis	No. of frames
LF	RF	LH	RH	LF	RF	LH	RH	LF	RF	LH	RH	LF	RF	LH	RH	LF	RF	LH	RH	LF-RF	LF-LH	LF-RH	RF-LH	LH-RH	RF-RH		
1	2	3	4	5	6	7	8	9	10	11	12	13	14	15	16	17	18	19	20	21	22	23	24	25	26	27	28

Table S3. Parameter description used in PCA calculations in Fig. 4 and Fig. S12. Related to Figure 4 and Figure 5.

Video recordings were analyzed in three walking speed categories (slow (less than 0.036 m/s), medium (0.036-0.072 m/s) and high (more than 0.072 m/s)). The numbers encode different parameters of the ellipsoids fitted to data points from 3D position analysis. LF: left front limb, RF: right front limb, LH: left hind limb, RH: right hind limb.

Supplementary Movies

Movie S1. Deep learning 3D movement analysis of a freely moving rat.

Movie S2. Spastic-paralyzed rat cannot use the left hindleg two days after chemical lesion of the pyramidal tract leading to one-sided circulation in the open-field test.

Movie S3. Spastic-paralyzed rat can start using his left hindleg 40 minutes after MPH-220 treatment due to relaxation of spasticity, which previously hindered forward progression of the leg during walking.

Movie S4. Pyramidal tract damaged rats fall over in the open field test due to spasticity-related abnormalities in leg positioning.

Movie S5. Spontaneous cramping occurs in the hindlegs of pyramidal tract damaged rats.

Movie S6. Open-field recordings of spastic rat from top and bottom views before and 3 hours after 20 mg/kg MPH-220 treatment.